Journal of Computational Neuroscience, 1, 167–194 (1994)

A Model of Selective Processing of Auditory-Nerve Inputs by Stellate Cells of the Antero-Ventral Cochlear Nucleus

YING-CHENG LAI,* RAIMOND L. WINSLOW, AND MURRAY B. SACHS lai@poincare.wbme.jhu.edu
Department of Biomedical Engineering, Center for Hearing Sciences,
The Johns Hopkins University School of Medicine, Baltimore, MD 21205

Received August 19, 1993; Revised February 2, 1994; Accepted (in revised form) February 17, 1994

Action Editor: Shihab Shamma

Abstract

Stellate cells in the cat antero-ventral cochlear nucleus (AVCN) maintain a robust rate-place representation of vowel spectra over a wide range of stimulus levels. This rate-place representation resembles that of low threshold, high spontaneous rate (SR) auditory nerve fibers (ANFs) *at low stimulus levels*, and that of high threshold, low-medium SR ANFs *at high stimulus levels*. One hypothesis accounting for this phenomenon is that AVCN stellate cells selectively process inputs from different SR population of ANFs in a level-dependent fashion. In this paper, we investigate a neural mechanism that can support selective processing of ANF inputs by stellate cells. We study a physiologically detailed compartmental model of stellate cells. The model reproduces PST histograms and rate-versus-level functions measured in real cells. These results indicate that simple and plausible distribution patterns of excitatory and inhibitory inputs within the stellate cell dendritic tree can support level dependent selective processing. Factors affecting selective processing are identified. This study thus represents a first step towards the development of a computational model of the AVCN stellate cell receptive field.

1 Introduction

The cochlear nucleus is the first central nucleus of the mammalian auditory system, receiving direct innervation from primary auditory nerve fibers (Osen 1970; Lorente de No 1981). The nucleus is divided into two major regions; the ventral and dorsal cochlear nuclei (VCN and DCN, respectively). The VCN is in turn partitioned into two sub-divisions; the antero-ventral and postero-ventral cochlear nuclei (AVCN and PVCN, respectively). At least seven principal cells may be defined on the basis of morphology within these subdivisions (Young et al. 1988b). These principal cells are: spherical bushy, globular bushy, and stellate cells in the AVCN; multipolar and octopus cells in the PVCN; and giant and fusiform cells in the DCN. While patterns of innervation differ considerably across cell type, in each case, principal cells receive synaptic input from either ascending or descending branches of incoming primary auditory nerve fibers (ANFs), local interneurons, neurons within different sub-nuclei of the cochlear nucleus, and from efferent fibers originating in higher auditory centers (Adams and Warr 1976; Cant and Morest 1978; Lorente de No 1981; Adams 1983).

Acoustic information from the auditory periphery undergoes processing within various sub-regions of the cochlear nucleus. These sub-nuclei in turn project in parallel to higher auditory centers. The cochlear nucleus therefore separates incoming acoustic information into several different processing streams, each of which may process different attributes of the acoustic stimulus. The functional importance of some of these output streams is beginning to be understood. The goal of our work is to investigate auditory processing in stellate cells of the AVCN.

*To whom correspondence should be addressed.

1.1 Morphology and Innervation of AVCN Stellate Cells

Stellate cells typically have from four to six long dendrites which exhibit little branching (Cant 1981; Rhode, Oertel and Smith 1983; Rouiller and Ryugo 1984). Electron microscopic reconstructions reveal occasional somatic spines (Cant 1981). The precise details of the spatial innervation pattern of stellate cell dendrites and soma by cochlear and non-cochlear synaptic inputs are unknown. The information which is available has been obtained from electron microscopic examination of soma and proximal dendrites (within about 100 μm from the soma; Cant 1981), and from tracing of HRP filled auditory nerve fibers to stellate cell soma (Liberman 1991). Two classes of cells may be defined according to the relative innervation density of proximal dendrites versus soma (Cant 1981). Type I stellate cells receive relatively few synaptic terminals on the soma; synaptic coverage is less than 30% of soma surface area. Type II cells receive much heavier somatic innervation (70% somatic coverage). Three different classes of vesicles are seen within the terminals of Type I cells: a) large spherical vesicles; b) small flattened vesicles; and c) small pleiomorphic vesicles. Terminals with the larger vesicles degenerate following cochlear ablation, whereas other terminals do not. This indicates that boutons with large spherical vesicles are from primary auditory nerve fibers, and the remaining boutons are non-cochlear in origin. Type II cells receive terminals containing vesicles similar in appearance to those seen on Type I cells. They are also innervated by terminals with large, flattened, disk shaped vesicles that survive cochlear ablation. The percentage of proximal dendritic and somatic surface covered by terminals containing round (presumably excitatory) versus flat or pleiomorphic (presumably inhibitory) vesicles is unknown.

Liberman has analyzed the projection patterns of high, medium, and low spontaneous rate (SR) fibers to different regions of the AVCN (Liberman 1991). This was done by recording from primary auditory-nerve fibers to determine their best frequency (BF) and SR, filling the fibers with HRP, then tracing labeled fibers to their sites of termination within the AVCN. Somatic inputs were defined as labeled terminals which were in close proximity to stellate cell bodies (defined using the criteria of Osen 1969 and Cant and Morest 1979). Non-somatic inputs were defined as terminals within the neuropil. Estimates of the number of low, medium, and high SR fiber somatic terminals were generated from these data. It was found that AVCN stellate cell soma receive more inputs from low-medium SR fibers than from high SR fibers (also see Fekete et al. 1982; Rouiller et al. 1986 and Ryugo and Rouiller 1988). The ratio of inputs differed from region to region, with virtually exclusive somatic innervation by low-medium SR fibers in the small cell cap region, a low-medium:high SR fiber terminal ratio of 8:1 in the anterior portion of the AVCN (AVCNa), and a ratio of about 1.25:1 in the posterior portion of the AVCN (AVCNp).

Little is known about the spatial projection patterns of high, medium, and low SR primary auditory-nerve fibers within stellate cell dendrites. Attempts are underway to correlate the morphology of synaptic endings of ANFs on stellate cell dendrites with input fiber SR (Berglund, Jacob and Liberman 1993; Ryugo, Wright and Pongstaporn 1993). Such correlations have not yet been established.

1.2 Response Properties of AVCN Stellate Cells

Stellate cells exhibit the so-called chopping response to BF tone bursts (Bourk 1976; Rhode, Oertel and Smith 1983; Rouiller and Ryugo 1984). This response is seen in post-stimulus time histograms (PSTHs), the distinguishing feature of which are multiple peaks due to the highly regular discharge properties of these cells. One way of quantifying regularity of discharge is to compute the ratio of the interspike interval standard deviation $\sigma_{isi}(t)$ to the mean value $\mu_{isi}(t)$ as a function of time during the stimulus interval (Bourk 1976; Young, Robert and Shofner 1988a; Young et al. 1988b), a measure of regularity known as the coefficient of variation $c_\sigma(t)$. A small $c_\sigma(t)$ value indicates that the mean interspike interval is large with respect to its standard deviation, and thus implies high regularity of discharge.

AVCN stellate cell responses may be divided into two major categories on the basis of plots of $\mu_{isi}(t)$ and $c_\sigma(t)$ in response to short BF tone bursts (Blackburn and Sachs 1989). Cells for which $\mu_{isi}(t)$ either remains constant or changes linearly in time, and which have an averaged $c_\sigma(t)$ value less than .3 are classified as sustained choppers (Chop-S); if the averaged $c_\sigma(t)$ value is greater than .3 the cells are classified as transient choppers (Chop-T). Cells for which

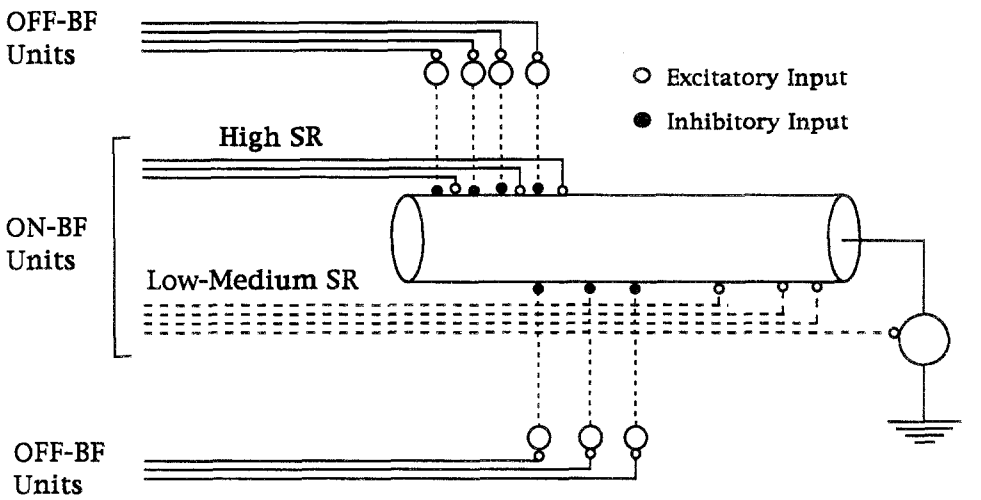

Fig. 1. A neural circuit for performing level-dependent selective processing based on the principle of on- versus off-path inhibition. See text for details.

$\mu_{isi}(t)$ increases abruptly to reach a plateau are also classifed as Chop-T cells. (A decision tree for classifying chopper cell responses is given in Fig. 1 of Blackburn and Sachs 1989.)

Temporal responses of AVCN stellate cells also differ from those of primary auditory-nerve fibers and AVCN bushy cells in that they exhibit virtually no phase-locked responses at frequencies greater than about 1.5 kHz (Blackburn and Sachs 1989; Bourk 1976). Phase-locking in stellate cells is limited by low-pass filtering of synaptic inputs to both soma and dendrites by a relatively large passive membrane time constant (about 7–10 *ms*) (Manis and Marx 1991; White 1990). This membrane time constant contributes to temporal integration of EPSPs. It is therefore likely that responses of stellate cells are determined primarily by the rate of arrival of synaptic inputs, and not their fine temporal structure.

AVCN cells may also be categorized according to features present in their response maps (plots of sound level and tone stimulus frequency pairs required to produce an increment or decrement of discharge rate). Most stellate cells exhibit response maps with central excitatory areas positioned about the unit's best frequency which are flanked by inhibitory areas above and/or below the BF (Young, Robert and Shofner 1988a; Shofner and Young 1985; Blackburn and Sachs 1992).

The representation of steady-state vowel spectra has been studied in the discharge patterns of both primary auditory-nerve fibers and the principal neurons of the VCN (Sachs and Young 1979; Young and Sachs 1979; Blackburn and Sachs 1990). Two theories describing the way in which the time-varying resonant frequencies of the vocal tract (formant frequencies) are encoded in the discharge patterns of auditory-nerve fibers have been proposed: the rate-place theory (Kiang and Moxon 1974; Sachs and Young 1979) and the temporal-place theory (Young and Sachs 1979). Both theories state that spectral information is encoded by the distribution of fiber response as a function of BF. Both are place theories since there is a precise relationship between fiber BF and place of origin along the basilar membrane. Place theories are supported by the observation that the tonotopic organization of the cochlea and auditory nerve is maintained throughout the central auditory system (Merzenich, Knight and Roth 1975). The two theories differ in the measure of ANF response used to encode spectral energy at each frequency (place). The rate-place theory states that spectral information is represented by the distribution of average discharge rate across fiber BF, whereas the temporal-place theory states that this information is encoded by the distribution of phase-locked responses.

Experiments aimed at measuring discharge patterns of large numbers of auditory-nerve fibers to acoustic stimuli (population studies) have demonstrated that temporal-place representations of acoustic spectra are robust, coding formant frequencies over a wide range of stimulus levels and signal-to-noise ratios (Sachs and Young 1979; Young and Sachs

1979; Costalupes 1985; Shofner and Sachs 1986). Population studies of the discharge patterns of AVCN stellate cells have demonstrated that these cells show virtually no phase-locked responses to vowel spectral peaks other than the first formant frequency. This is a result of the high degree of temporal integration of EPSPs in these cells.

Rate-place representations derived from responses of auditory-nerve fibers are also capable of encoding stimulus spectra over a wide range of sound levels. This was demonstrated by Sachs and Young (1979) in their studies of rate-place representations of ANF responses to the steady-state vowel /ɛ/. Specifically, such representations computed from responses of low-threshold, high SR ANF's encode vowel formant frequencies at low stimulus levels (Sachs and Young 1979). However, because of the combined effects of rate saturation and two-tone suppression, formant peaks present in rate-place representations derived from responses of high SR ANFs disappear at moderate to high stimulus levels. At these higher stimulus levels, formant peaks are maintained in representations derived from the responses of high threshold low SR fibers.

Blackburn and Sachs (1990) measured rate-place representations of steady-state vowel spectra in the responses of AVCN stellate cells. They showed that these cells maintain peaks in discharge rate corresponding to vowel formant frequencies over a broad range of stimulus levels; a finding especially true of the Chop-T cells. At low stimulus levels, rate-place representations computed from responses of the Chop-T cells appeared similar in shape to those computed from responses of low threshold high SR primary ANFs. At high stimulus levels, rate-place profiles for the Chop-T cells were similar to those computed from high threshold low SR fibers (Fig. 19, Blackburn and Sachs 1990). These data suggest that stellate cells perform a level-dependent selective processing of ANF inputs, an hypothesis presented previously on the basis of theoretical considerations (Winslow, Barta and Sachs 1987).

1.3 Objectives

At present, computational models of stellate cells provide the only means for testing hypotheses about the innervation of stellate cell dendrites by primary auditory-nerve fibers. To be successful, such models must reproduce known response properties of these cells (primarily responses to BF tone bursts of varying level) as well as account for level-dependent selective processing of ANF inputs. In this paper, we present a first step in this direction by describing a model of stellate cells that reproduces PST histograms and rate-level functions (plots of discharge rate versus BF tone level) measured in real cells, and which performs selective processing.

The starting point of this analysis is an hypothesized neural mechanism for performing level-dependent selective processing (Winslow, Barta and Sachs 1987). The circuit is based on the principle of on- versus off-path inhibition (Koch, Poggio and Torre 1982; Koch and Poggio 1986), and is illustrated in Fig. 1. In its initial form, high SR, low threshold auditory nerve fibers with BF determining that of the target stellate cell are assumed to project to distal regions of the dendritic tree, where they form excitatory synapses. Higher threshold, low-medium SR fibers from the same BF region are assumed to form excitatory synapses on the proximal dendrites and soma of the same cell. Off-BF auditory nerve fibers are assumed to project to interneurons which in turn form inhibitory synapses on the target stellate cell. These inputs are located on the direct path that current must take when flowing from the distal synapses to the soma. This situation is referred to as on-path inhibition. No constraints are placed on the type of ANF inputs to the inhibitory interneurons other than it must include high SR fibers. The reversal potential of the inhibitory ionic species is assumed to be equal to the resting potential of the cell (shunting inhibition). Under these assumptions, it was conjectured that at low stimulus levels only the low threshold high SR on-BF fibers would be activated, thus driving the responses of the second order stellate cell. Low SR, on-BF fibers would not be activated due to their higher acoustic thresholds. As stimulus intensity increased, spread of excitation along the basilar membrane would result in activation of the off-BF fibers, providing on-path inhibitory inputs (via interneurons) to the target stellate cell. On-path inhibitory inputs of the shunting type are very effective in preventing current from more distal regions from reaching the soma, but ineffective in reducing somatic response to synaptic currents positioned more proximally (referred to as off-path inhibition) (Koch, Poggio and Torre 1982). Thus, at stimulus levels high enough to activate inputs from off-BF fibers, synaptic current

from more distal synapses would be shunted through the dendritic membrane, allowing currents from more proximally located low-medium SR fiber synapses to drive the cell.

Such a synaptic arrangement in the model is consistent with existing data in that:

- off-BF inhibition accounts for inhibitory sidebands seen in response maps of AVCN stellate cells (Young, Robert and Shofner 1988a; Shofner and Young 1985; Blackburn and Sachs 1992);
- inhibition mediated by a single interneuron is indicated by the roughly one synaptic time delay observed between EPSPs and IPSPs in stellate cells from the cochlear nucleus slice preparation (Oertel 1983);
- inhibition is of the shunting type, since the reversal potential of IPSPs measured in stellate cells is equal or close to the cell resting potential, and is mediated by an increase in conductance of chloride ions (Oertel 1983; Wu and Oertel 1986);
- stellate cells receive excitatory inputs from primary auditory nerve fibers of all SR categories (Young and Sachs 1988; Liberman 1991).

The hypothesis remains speculative in that nothing is known about the precise spatial arrangment of excitatory and inhibitory synaptic inputs within the stellate cell dendritic tree.

We will use the hypothesis described above as a starting point for analyses of possible innervation patterns of AVCN stellate cells. We will determine whether or not such a model of innervation can account for responses of these cells to BF tone bursts as well as perform selective processing of ANF inputs, as described by Blackburn and Sachs (1990).

2 Excitatory and Inhibitory Interactions in a Passive Stellate Cell Model

2.1 Steady-State Analyses

We begin our studies of selective processing of auditory-nerve fiber inputs to stellate cells by investigating the nature of interactions between steady-state excitatory and inhibitory conductance inputs in a simple cable model of an AVCN stellate cell using methods described previously by Rall (1964, 1977) and Koch et al. (Koch, Poggio and Torre 1982; Koch and Poggio 1986). The cable model of stellate cells used in this study is identical to that used by Banks and Sachs (1991). The model consists of a passive uniform cylinder with electrotonic length L=1, terminated by a parallel RC circuit modeling the passive soma. The soma membrane conductance G_m was computed assuming a spherical soma diameter of $25\mu m$ and a specific membrane resistance of 10,000 Ω-cm^2. The resulting input resistance ($510M\Omega$) and membrane time constant (10 ms with specific membrane capacitance $C_m = 1uF/cm^2$) are within the range measured by whole-cell recording in enzymatically dissociated stellate cells from guinea pig VCN (447 ± 265 MΩ; Manis and Marx, 1991). Axial resistance R_i was set to 150Ω-cm. Synaptic inputs are modeled as maintained conductances in series with batteries representing reversal potentials. Inhibition in stellate cells of the cochlear nucleus slice preparation is known to be mediated by changes in membrane permeability to chloride ions. The reversal potential of this inhibition (E_i) is equal to or near the cell resting potential E_r (Wu and Oertel 1984; Wu and Oertel 1986). We therefore model inhibition as the shunting type ($E_i = E_r$).

Passive linear cable theory can be used to derive analytic expressions for the steady-state voltage at the soma in response to maintained excitatory input, both with and without inhibition (Rall 1977). Interactions between maintained excitatory and inhibitory conductance inputs are quantified by defining an attenuation factor G as the ratio of voltage at the soma in response to simultaneous excitation and inhibition, to voltage at the soma in response to excitation alone (Koch, Poggio and Torre 1982). We have examined the dependence of G on the absolute and relative amplitudes of steady-state excitatory and inhibitory conductances using this equivalent cylinder model. In the first test, a fixed amplitude excitatory conductance is applied at dendritic location $L_e = 1$. Four test values of G_e were selected in order to produce supra-threshold ($G_e = 1$ nS), half-saturating ($G_e = 18$ nS), near saturating ($G_e = 316$ nS), and saturating ($G_e = 5600$ nS) voltage responses. The value of G was then calculated as the location and amplitude of on-path inhibition was varied. Since our findings from this study are similar to these of Koch et al. (1982), we will omit presentation of the data, and instead summarize our results.

For a saturating excitatory conductance change, on-path shunting inhibition becomes increasingly ef-

fective as it is positioned closer to the soma. This is true even when the inhibitory conductance is comparable in magnitude to, or smaller than, the excitatory conductance. For the case of a near saturating excitatory synaptic input, shunting inhibition becomes more effective as the site of inhibition moves towards the soma. However, in this case, inhibition must be at least one order of magnitude larger than excitation in order for a powerful shunting effect to occur. In general, as the magnitude of the excitatory conductance is decreased, the magnitude of the inhibitory conductance must be increased relative to the size of the excitatory conductance in order to achieve a given level of attenuation. As the excitatory conductance amplitude is decreased to half-saturating and supra-threshold values, all on-path sites of inhibition become nearly equally effective. While the optimal site of inhibition is at the site of excitation (Koch et al. 1982), the observed dependence of G on the spatial location of inhibition is not very significant. As the amplitude of the excitatory conductance decreases, the inhibitory conductance amplitude must be made significantly larger than the excitatory conductance in order for shunting inhibition to have a powerful effect. These results have been verified by repeating the on-path calculations for different sites of excitatory input.

We have also computed G factors when shunting inhibitory input is located off-path. As the magnitude of the excitatory conductance is decreased, the effectiveness of off-path shunting inhibition increases. As before, the magnitude of inhibition relative to excitation required to produce a shunting effect also increases as the amplitude of the excitatory conductance decreases.

2.2 *Transient Analyses*

This section presents numerical results for the case where both excitatory and inhibitory synapses induce conductance changes $g_{e,i}(t)$ modeled as time-varying α-functions (Rall 1964) of the form,

$$g_{e,i}(t) = G_{e,i}\frac{t - t_0}{t_p^{e,i}} e^{\left[1-\frac{t-t_0}{t_p^{e,i}}\right]}. \qquad (1)$$

In the above equation, G_e and G_i are the peak amplitudes of the excitatory and inhibitory conductance changes, t_0 is the occurrence time of the synaptic input, and, $t_p^{e,i}$ is the time relative to t_0 when the conductance change reaches its maximum (time to peak).

Transient analyses are performed using four combinations of (G_e, G_i) values for which on-path shunting inhibition is highly effective in the steady state case. G_e is chosen to produce supra-threshold, half-saturating, near-saturating and saturating local voltage responses, as described in Sec. 2.1. values of G_i are chosen to produce significant attenuation based on the general finding of Sec. 2.1: in the steady-state, as the magnitude of the excitatory conductance is decreased, the magnitude of the inhibitory conductance must be increased relative to the size of the excitatory conductance in order to achieve an effective attenuation of soma voltage response. Accordingly, G_i is set equal to $1000 * G_e$, $100 * G_e$, $10 * G_e$ and G_e for supra-threshold, half-saturating, near-saturating and saturating voltage responses, respectively. The value of t_p^e is set to 0.25 *ms* (Banks and Sachs, 1991) so that the excitatory post stimulus potentials (EPSPs) have halfwidths comparable with those reported in stellate cells of the cochlear nucleus slice preparation (3–4 *ms*) (Wu and Oertel 1984; Wu and Oertel 1986; Oertel, Wu and Hirsch 1988). There are no precise estimates of the half-width of IPSPs, but they are clearly larger than those for EPSPs (Wu and Oertel 1984). Time to peak of the inhibitory conductance change t_p^i is therefore varied over the range from 0.25 to 2 *ms*.

Effects of shunting inhibition on soma voltage response are again characterized using the G factor. However, for the transient case, G values will be different when inhibition occurs at different delay times Δt with respect to the occurrence time of excitation, where positive values of Δt indicate that the occurence time of inhibition is delayed relative to that of excitation. The attenuation factor is therefore written as $G(\Delta t)$.

Features of $G(\Delta t)$ have been analyzed by Koch and Poggio (1986) using the δ-ganglion cell of the cat retina as a model. In general: a) $G(\Delta t) \rightarrow 1$ if $\Delta t \ll 0$ or $\Delta t \gg 0$; and b) $G(\Delta t)$ attains a minimum value G_{min} for some Δt_{min}. The half width of the $G(\Delta t)$ function is defined as $T_G = \Delta t^+ - \Delta t^-$, where $G(\Delta t^+) = G(\Delta t^-) = (1\text{-}G_{min})/2$ and $\Delta t^+ > \Delta t^-$. While G_{min} characterizes the maximum extent to which the soma excitatory voltage response can be suppressed by the shunting inhibition, T_G quantifies the

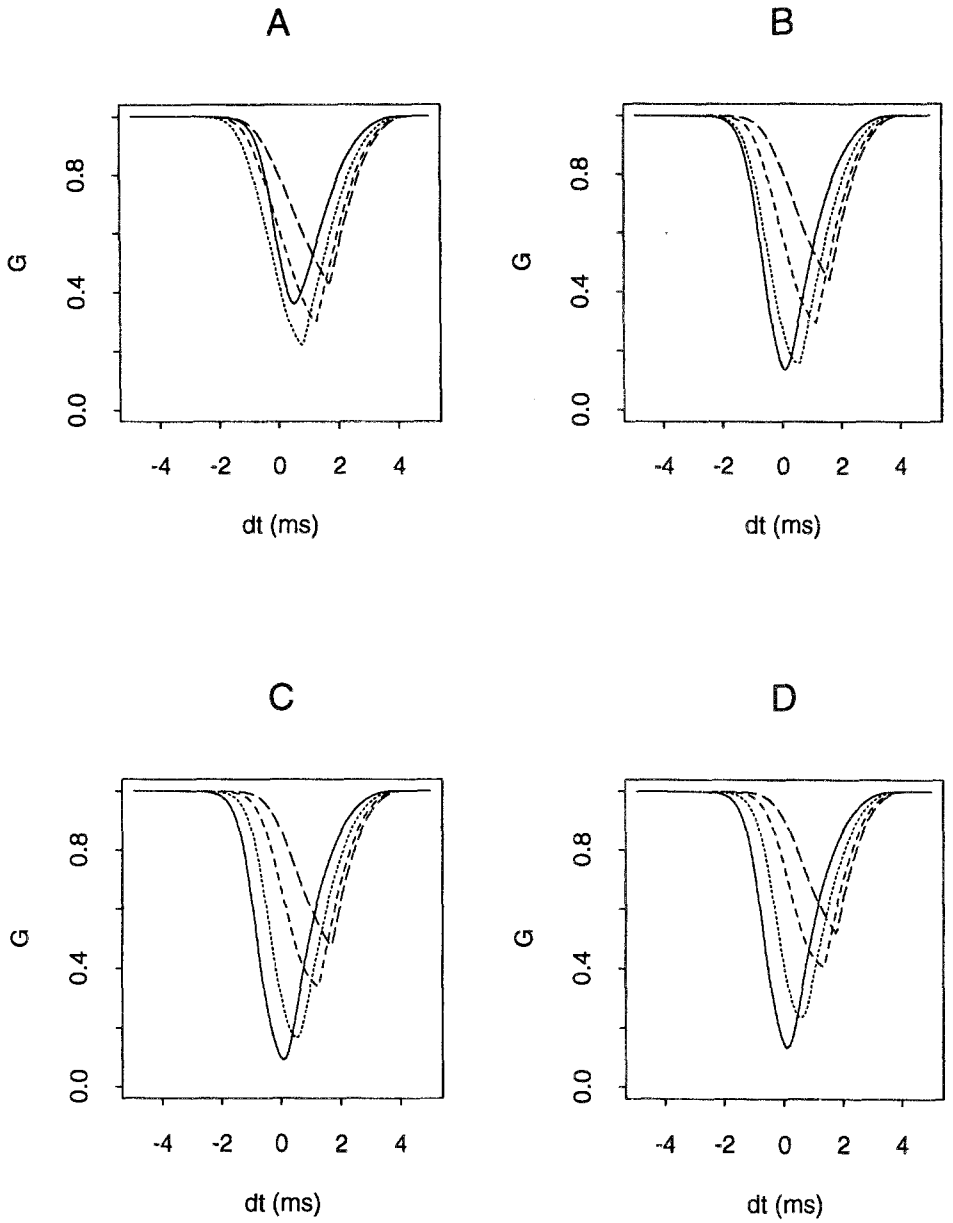

Fig. 2. The effect of on-path shunting inhibition when both excitatory and inhibitory synapses induce time-varying conductance changes. The functions $G(\Delta t)$ are plotted for the saturating ($G_e = G_i = 5600nS$, A), near-saturating ($G_e = 316nS$, $G_i = 10G_e$, B), half-saturating ($G_e = 18nS$, $G_i = 100G_e$, C), and supra-threshold ($G_e = 1nS$, $G_i = 1000G_e$, D) voltage response regimes. The times to peak for excitation and inhibition are $t_p^e = t_p^i = 0.25ms$. Four curves in each figure A–D correspond to four on-path locations of inhibition (the site of excitation is fixed at $L_e = 1$): $L_i = 1$ (solid lines), $L_i = 0.75$ (dotted lines), $L_i = 0.5$ (dashed lines) and $L_i = 0.25$ (long dashed lines). For half-saturating and supra-threshold regimes (C and D, respectively), the optimal location of inhibition to veto excitation is at the site of excitation. While for saturating and near-saturating regimes (A and B, respectively), the optimal inhibition location moves slightly away to a location around $L_i = 0.75$.

range of time delays between excitation and inhibition over which soma voltage response can be effectively attenuated.

2.2.1 Effects of On-Path Inhibition Figures 2A–D show $G(\Delta t)$ for saturating (A), half-saturating (B), near-saturating (C), and supra-threshold (D) excita-

tory conductance inputs. The time to peak of inhibition is set to $t_p^i = 0.25ms$. In each panel, excitation is applied at electrotonic location $L_e = 1$. The four curves in each figure represent cases where shunting inhibition is applied at $L_i = 1$ (solid line), 0.75 (dotted line), 0.5 (short-dashed), and 0.25 (long-dashed line). These data demonstrate that:

A. There exists a window of Δt values, characterized by the half-width T_G of the $G(\Delta t)$ function, within which shunting inhibition is effective (Koch, Poggio and Torre 1982; Koch and Poggio 1986). For the curves in Figs. 2A–D, T_G is about 2 ms.

B. For half-saturating and supra-threshold regimes (G_e=1 and 18nS, Figs. 2C and 2D, respectively), the optimal location of inhibition for vetoing excitation is at the site of excitation;

C. As the amplitude of the excitatory conductance change increases to the saturating and near-saturating regimes (G_e=316 and 5600nS, Figs. 2A and 2B, respectively), the optimal location for inhibition moves away from the site of excitation to about $L_i = 0.75$. As L_i becomes smaller than 0.75, effectiveness of inhibition is reduced. This is in contrast to the steady-state case where the optimal location of inhibition continues to shift towards the soma as the magnitude of the excitatory conductance changes increase;

D. As the distance between excitation and inhibition increases, the value of Δt_{min} increases;

E. $G(\Delta t)$ curves fall slowly for $\Delta t < \Delta t_{min}$ and rise relatively rapidly for $\Delta t > \Delta t_{min}$. This can be understood by noting that for $\Delta t > \Delta t_{min}$, the excitatory response has propagated past the site of inhibition before the inhibitory conductance change occurs, rendering inhibition highly ineffective.

2.2.2 Effects of Off-Path Inhibition Figures 3A–D show $G(\Delta t)$ functions for the same regimes described above. In each figure, the site of excitation is fixed at $L_e = 0$ (on soma) and L_i is set to 0.0 (solid line), 0.25 (dotted line), 0.5 (short-dashed line), and 0.75 (long-dashed line). The time to peak for excitation and inhibition is the same as in Figs. 2A–D. For all cases of off-path inhibition, $G(\Delta t)$ is large (generally greater than 0.85), indicating that inhibition is much less effective at attenuating the soma excitatory voltage responses when positioned off-path. Moving inhibition away from the site of excitation reduces the effect of shunting inhibition substantially. In particular, for $L_i \geq 0.25$, we have $G \rightarrow 1$ and, hence, inhibition has virtually no effect on vetoing excitation.

2.2.3 Effect of the Time to Peak of Inhibition The effectiveness of on-path shunting inhibition depends sensitively on the value of t_p^i. This is important because precise values for t_p^i have not been measured for stellate cell IPSPs. Figures 4A and B show $log_{10}G_{min}$ and T_G as a function of t_p^i. Excitatory and inhibitory conductance magnitudes are fixed at G_e = 18nS (the half-saturating case) and $G_i = 100G_e$. Excitatory input is placed at $L_e = 1$ and the attenuation factor is calculated for the case where inhibition is at its optimal location to veto excitation ($L_i = L_e$ within the half-saturating regime). These data show that G_{min} decreases rapidly with increasing time to peak values t_p^i. Increasing t_p^i to about 1 ms produces a near maximum attenuation of soma response. Figure 4B shows that the degree of temporal coincidence required for attenuation of somatic response decreases linearly with t_p^i. Similar $log_{10}G_{min}$ and T_G versus t_p^i curves were obtained for an excitatory synaptic conductance magnitude within the saturating regime.

2.3 Summary of Steady-State and Transient Analyses

The half-saturating excitatory conductance change (18nS) used in the above analyses is similar in magnitude to the conductance change (G_e=26nS) used previously in the Banks-Sachs model (1991). Excitatory conductance changes of this or smaller magnitude are required to produce the characteristic PSTH chopping pattern of AVCN stellate cells (Banks and Sachs 1991), and to account for experimentally measured phase-locked responses (Wang 1991). For excitatory inputs of this magnitude or lower, both the steady-state and transient analyses show that the optimal site of inhibition is at the site of excitation. This suggests a simplification of the selective processing hypothesis presented in Sect. 1.3 in which inhibitory inputs may be co-located with the excitatory inputs. Inhibition will have little effect on more proximal excitation as long as the electrotonic distance between the two input sites is at least .25 space constants.

The simulation data also show that temporal coincidence is required for effective shunting of excitatory inputs by inhibitory inputs in the on-path case. While the need for temporal coincidence is reduced as the time-to-peak of inhibitory inputs is increased,

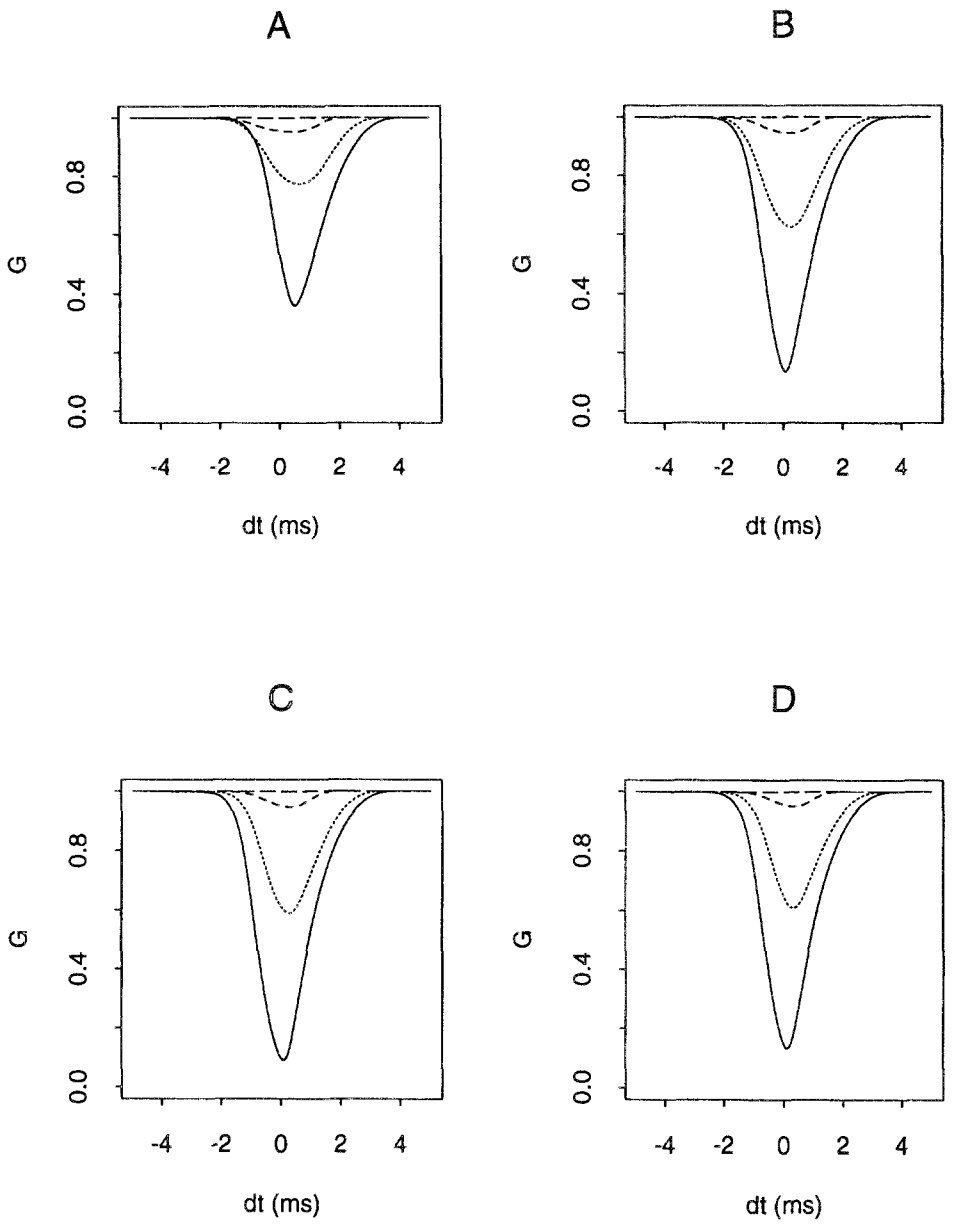

Fig. 3. The effect of off-path inhibition. Four curves in A-D correspond to four locations of inhibition [the site of excitation is fixed at $L_e = 0$ (soma)]. They are: $L_i = 0$ (solid lines), $L_i = 0.25$ (dotted lines), $L_i = 0.5$ (dashed lines) and $L_i = 0.75$ (long dashed lines). Clearly, in all four voltage response regimes, the off-path inhibition is highly ineffective at reducing the soma excitatory voltage response. As inhibition moves away from excitation beyond $L_i = 0.5$, the inhibition has virtually no effect on the excitation ($G \rightarrow 1$ for $L_i \geq 0.5$).

this brings into question the effectiveness of on-path inhibition when there is no deterministic temporal relationship between the times of occurrence of excitatory and inhibitory inputs. This is the case when the discharge patterns of auditory-nerve fibers (and those of the inhibitory interneuron as well) are modeled as stochastic processes.

3 Selective Processing in an Active Stellate Cell Model

3.1 Numerical Procedures

In this section, we incorporate a somatic spike generator into the passive cable model described in Sect. 2.1.

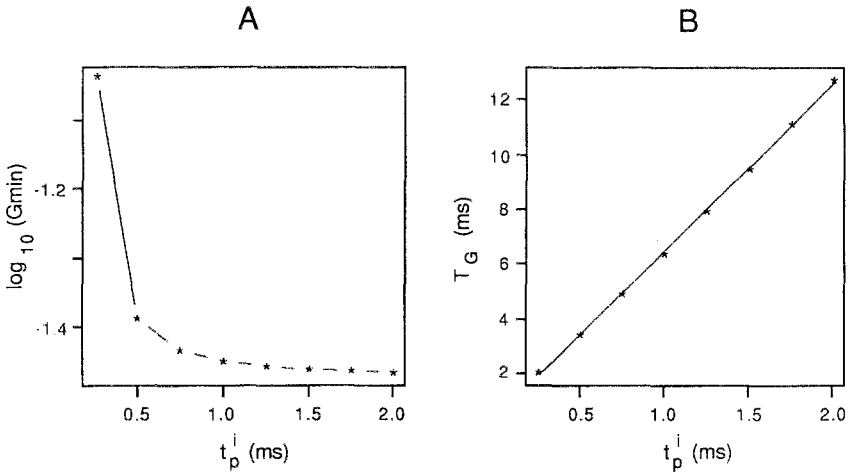

Fig. 4. For a case in the half-saturating regime, (A) The minimum G value G_{min} and, (B) the half width of the G function T_G versus the time to peak of inhibition t_p^i. Note that G_{min} versus t_p^i is highly nonlinear and, G_{min} decreases rapidly if t_p^i is increased slightly above $0.25ms$. The relation between T_G and t_p^i is linear (B).

Addition of a spike generator makes it possible to compute the discharge pattern of model stellate cells in response to simulated excitatory and inhibitory synaptic inputs with event times modeled as random point processes.

We have used the spike generator model (Hudgkin-Huxley type of ionic channel dynamics) of Banks and Sachs (1991) with the modification proposed by Wang (1991) in which the thresholds of all steady-state activation and inactivation functions are shifted in the depolarizing direction by 9mv. This shift is required to fit the relationship between input current magnitude and stellate cell firing rate, as measured by Oertel (Wang 1991).

Occurrence times of excitatory synaptic inputs are modeled using dead-time modified inhomogeneous Poisson counting processes (IPCPs) (with dead time $t_d = 0.7ms$) (Barta and Young 1986; Rothman 1991) Such an input model approximates the response of non-phase-locked high-BF ANFs to BF tone bursts. The spike train model is specified by an instantaneous rate function $\lambda(t)$. Since the instantaneous discharge rate of ANFs to tone bursts is a rapidly adapting function of time, $\lambda(t)$ is chosen to reflect such adaptation. Specifically, $\lambda(t)$ can be written as (Gaumond, Molnar and Kim 1982; Johnson and Swami 1983; Rothman 1991),

$$\lambda(t) = (1-e^{-t/t_q})(R_\tau e^{-t/t_r} + R_{st}e^{-t/t_{st}} + R_{ss})r(t-t_{-1}) \quad (2)$$

The first term in Eq. (2) simulates the exponential rise in firing rate at tone burst onset, the second term simulates the exponential decay of discharge rate to a steady-state value during the burst (Westerman and Smith 1984). Time constants t_q, t_r, t_{st} and rate constants R_r, R_{st}, and R_{ss} are adjusted to produce PSTHs with shapes and first-spike latencies similar to those of ANFs. The function $r(t-t_{-1})$ is a refractory function describing the recovery of firing probability as a function of time after the previous spike occurrence at time t_{-1}. It is estimated from hazard functions measured in primary auditory-nerve fibers (Li 1991):

$$r(t-t_{-1}) = \begin{cases} 1-e^{-\nu(t-t_{-1}-t_d)} & \text{if } t-t_{-1} \le t_d \\ 0 & \text{otherwise} \end{cases}, \quad (3)$$

where ν is a constant that can be obtained based on ANF's discharge rate (Li 1991). Spike occurrence times for different SR populations can be generated given $\lambda(t)$ (Gaumond, Molnar and Kim 1982; Johnson and Swami 1983; Barta and Young 1986; Li 1991; Rothman 1991). Parameter values used to generate realizations of event times for the low and high SR ANF spike train models used in this study are summarized in Table 1.

Figures 5A–B show simulated PSTHs for model high SR and low SR ANF inputs computed using the instantaneous rate function defined by Eqs. (2)–(3). PSTHs were computed by dividing the duration of the stimulus interval (120 ms) into 500 bins and by accumulating the number of spikes in each bin for

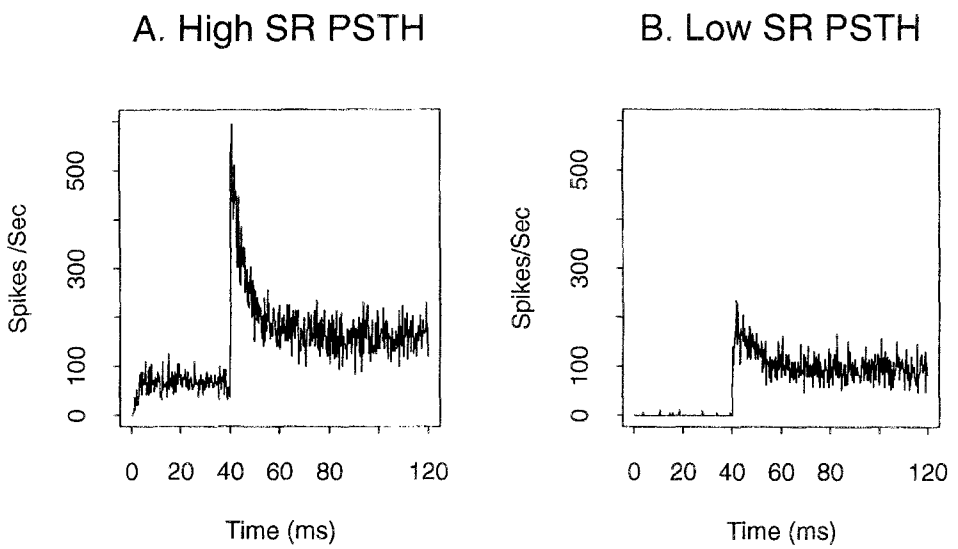

Fig. 5. PSTHs of typical low-threshold, high SR ANFs (A) and high threshold, low-medium SR ANFs (B) used in our computations. These ANF spike trains are generated using the model by Rothman (1991, also see text for details). The average maintained rates for high SR and low-medium SR ANFs are 160 spikes/s and 100 spikes/s, respectively. Each spike train has a length of 120 *ms*, where the first 40 *ms* interval simulates the spontaneous activities of ANFs. We choose $SR = 68$ spikes/s and $SR = 0.5$ spikes/s for high SR and low-medium SR fibers, respectively.

Table 1. Parameter values used in the model of Sec. 3.1 for generating high SR and low-medium SR ANF spike trains.

Quantities	High SR ANF	Low-Medium SR ANF
t_q (*ms*)	0.2	1.5
t_r (*ms*)	3.0	2.0
t_{st} (*ms*)	10.0	10.0
ν (1/*ms*)	2.0	2.0
R_r (spikes/*ms*)	0.6	0.33
R_{st} (spikes/*ms*)	0.2	0.11
R_{ss} (spikes/*ms*)	0.2	0.11

800 statistically independent realizations of the input spike train. Spike rate during the initial 40 *ms* interval corresponds to the spontaneous discharge rate of the model ANF (68 spikes/s for the high SR fiber in A; .5 spikes/s for the low SR fiber in B). The increase in discharge rate at t=40 *ms* corresponds to onset of an 80 *ms* tone burst. The maintained rate to the tone (steady-state driven rate plus spontaneous rate) is 160 and 100 spikes/s for the high and low SR model fibers, respectively. The high degree of irregularity in the occurrence time of ANF spikes can be characterized by plots of interspike interval, standard deviation, and coefficient of variation. Plots generated from the data shown in Figs. 5A–B agree well with those measured experimentally in primary auditory-nerve fibers (Rothman 1991; Li 1991).

The times of occurrence of excitatory synaptic inputs to the model stellate cell were simulated using the point process models described above. Each excitatory event evoked a membrane conductance change of the form given by Eq. (1), with time to peak t_p^e set to 250 μsec. Conductance changes evoked by sequential events at the same synapse were summed linearly. Multiple inputs from different ANF's to the stellate cell were modeled as statistically independent realizations of dead-time modified IPCPs (Johnson and Kiang 1976). Since nothing is known about the firing patterns of the inhibitory interneurons which provide inputs to AVCN stellate cells, we have accepted the simplest possible assumption that these inhibitory interneurons have the same stochastic discharge patterns and adaptation characteristics as do primary ANFs which drive them. Conductance changes evoked by inhibitory inputs were modeled as described for excitatory inputs.

The passive cable modeling the stellate cell dendritic tree was partitioned into 20 compartments, with

compartment 1 corresponding to the distal end of the cable and compartment 20 corresponding to the proximal end next to the soma. The soma is denoted by compartment 21. As in Banks and Sachs (1991), a single spike generating axonal compartment was added to the model. The dendritic cable was also divided into distal and proximal regions. Assuming a cable length of $600\mu m$ (Banks and Sachs 1991), each compartment has physical length $30\mu m$. The 4 compartments modeling the $120\mu m$ length of the cable nearest to the soma are defined as the proximal region. The proximal region is therefore 0.2 space constants in length and corresponds to the region studied by Cant (1981). The remainder of the cable is defined as the distal region. This choice of proximal region is rather arbitrary. As will be shown, the relative length of proximal and distal regions is an important parameter influencing the shape of model stellate cell rate-level functions.

PSTHs were computed for model stellate cells as described previously for ANFs. For each input configuration, stellate cell somatic action potentials were computed in response to 800 statistically independent realizations of the firing patterns of the input ensemble. Event times for model stellate cells were computed as the time at which somatic membrane potential crossed a 0 mV threshold value in the positive direction. PSTHs were computed using these event times. Plots of $\mu_{isi}(t)$ and $c_\sigma(t)$ were computed as described by Young et al. (1988). Plots of PSTH, $\mu_{isi}(t)$ and $c_\sigma(t)$ were smoothed with a moving triangular window of width 1.68 *ms*.

3.2 Properties of Stochastic Inhibition

3.2.1 Effects of Stochastic On-Path Inhibition According to the selective processing hypothesis, at stimulus levels within 10–15 dB of threshold, responses of stellate cells are dominated by inputs from distally positioned high SR ANF inputs. In order to simulate this situation, a single high SR ANF input was applied to each of the 16 distal compartments. Each model ANF was assumed to have an SR of 68 spikes/s, and a driven rate (the difference between total discharge rate and spontaneous rate) in response to a BF tone of 57 spikes/s. Stimulus onset of an 80 *ms* tone burst occurs at 40 *ms*. The magnitude of each excitatory conductance change was set to $G_e = 6G_0$ ($G_0 \approx 1.3$nS, Wang, 1991), where G_0 is the total membrane conductance of a single compartment.

The resulting PSTH (limited to the first 80 *ms*) is shown in Fig. 6A. The model stellate cell has a spontaneous discharge rate of zero, despite the fact that there are 16 high SR ANFs each with a spontaneous rate of 68 spikes/s applied to its distal dendritic tree. This is consistent with the observation that 60% of all AVCN stellate cells have SR less than 1 spike/sec, and 45% have zero spontaneous rate (Blackburn and Sachs 1989). The model cell PSTH also shows the distinctive chopping pattern characteristic of these cells during the first 20 *ms* after tone onset, after which the firing rate reaches a steady value of about 78 spikes/s.

Figures 6B–D show plots of $\mu_{isi}(t)$, $\sigma_{isi}(t)$ and $c_\sigma(t)$, respectively. These three quantities increase abruptly following stimulus onset to reach a plateau value. The steady state value of $c_\sigma(t)$ is .62 (averaged over 60–80 *ms*). This response of the model cell is therefore classified as Chop-T according to the criteria of Blackburn and Sachs (1989).

We next increase the driven rate of each high SR fiber to a saturating discharge rate of 92 spikes/s. The resulting response is shown in Figs. 7A–D. The PSTH in Fig. 7A again shows an initial period of chopping, leading to a steady-state discharge rate of 124 spikes/s. Plots of $\mu_{isi}(t)$ (Fig. 7B), $\sigma_{isi}(t)$ (Fig. 7C) and $c_\sigma(t)$ (Fig. 7D) also increase abruptly during the initial stimulus interval to reach plateau values, with the averaged $c_\sigma(t)$ value being .41 (during 60–80 *ms*). The response of this unit, which receives only distal dendritic innervation by high SR ANF inputs, is classified as Chop-T at both near threshold and saturating stimulus levels.

The nature of chopping depends on the extent of convergence of ANF inputs and on the magnitude of the synaptic conductance change evoked by each input. As an example, for the input configuration of Figs. 6–7, 2 high SR ANF inputs to $C1$–$C16$ with a conductance value of $Ge = 4G_0$ gives rise to a chopping PSTH response with an average $c_\sigma(t)$ value of 0.16, while 3 high SR ANF inputs with $G_e = 3G_0$ generates a chopping response with average $c_\sigma(t)$ of 0.12. In both these cases, responses can be classified as slowly adapting chopping responses (data not shown).

Figures 8A–B illustrates the ability of stochastic shunting inhibitory inputs to veto the excitatory response of the model stellate cell shown in Fig. 7.

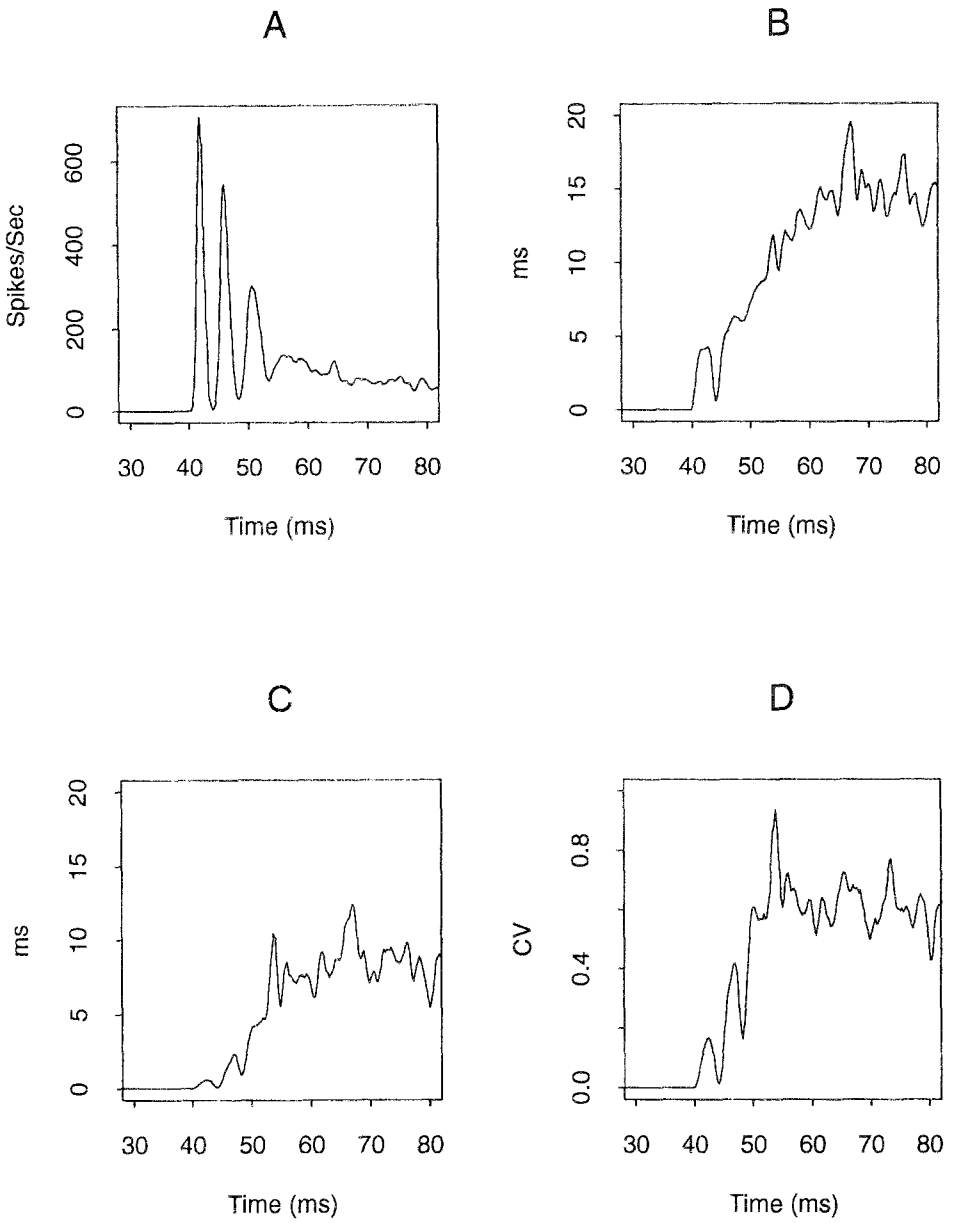

Fig. 6. Plots of PSTH (A), $\mu_{isi}(t)$ (B), $\sigma_{isi}(t)$ (C) and $C_\sigma(t)$ (D) of the model cell response when one half-saturating high SR fiber (with an average maintained rate of 125 spikes/s) is applied to each distal compartment $C1$–$C16$ with $G_e = 6G_0$, where G_0 is the membrane conductance for a single compartment ($G_0 \approx 1.3nS$). This excitatory conductance amplitude is fixed for subsequent similar figures in this paper. The resulting average discharge rate and average $C_\sigma(t)$ in the time interval $[60ms, 80ms]$ are 78 spikes/s and 0.62, respectively. The response can be classified as Chop-T. Plots in A–D are smoothed using a moving triangle filter with a window of 1.68 *ms* (same for subsequent similar plots in this paper).

According to the steady-state and transient analysis in Sec. 2.1–2.2, when G_e is in the half-saturating and supra-threshold regimes, shunting inhibitory input is most effective when co-located with excitation. The data of Fig. 8 show the effect of stochastic shunting inhibition when 1 inhibitory input is placed at each of the distal 16 compartments, with t_p^i=1 *ms* and G_i=80G_0 for each input. The configuration of excitatory inputs is the same as described for Fig. 7. Both excitation and inhibition are turned on at t=40

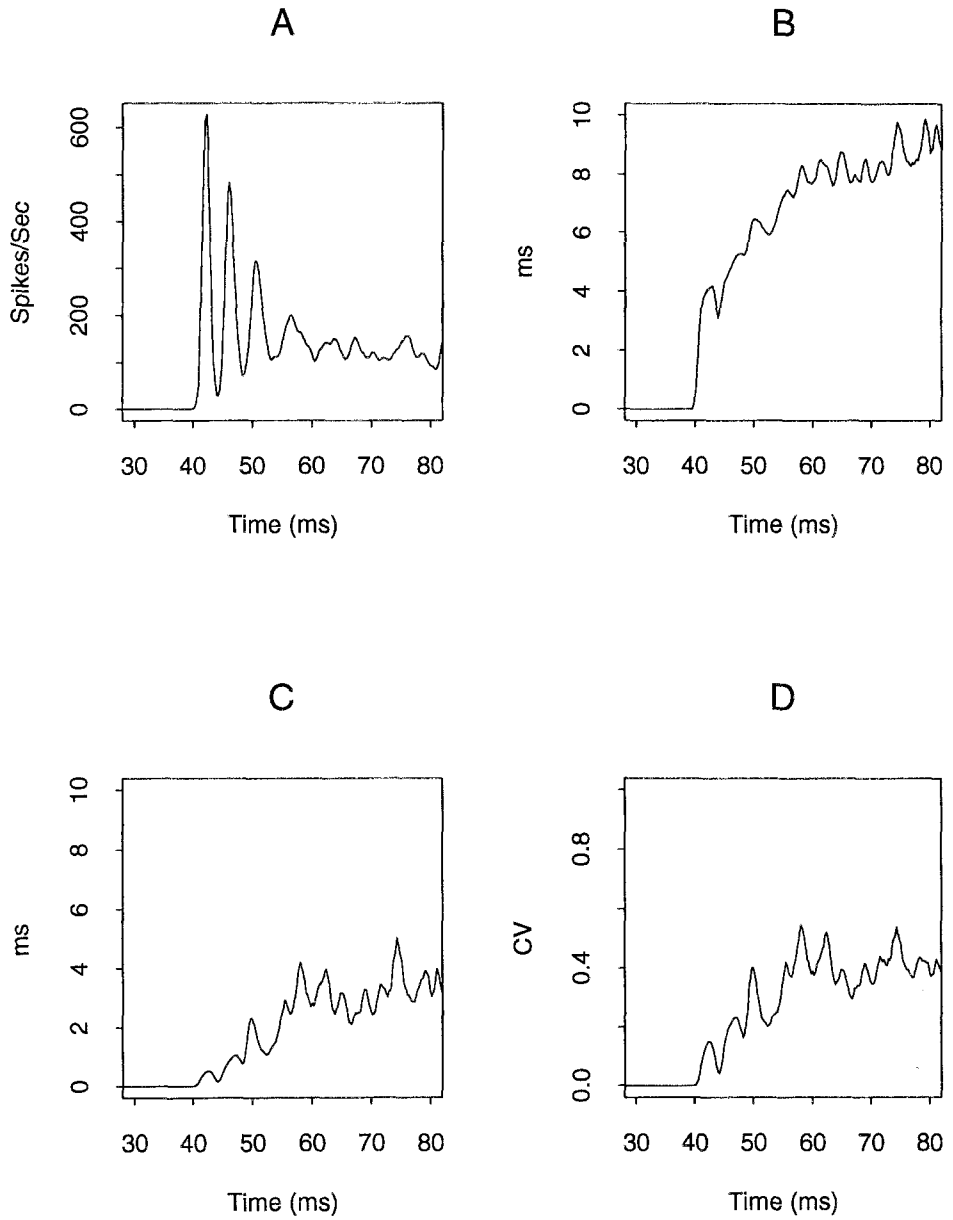

Fig. 7. Plots of PSTH (A), $\mu_{isi}(t)$ (B), $\sigma_{isi}(t)$ (C) and $C_\sigma(t)$ (D) of the model cell response when one saturating high SR fiber (with an average maintained rate of 160 spikes/s) is applied to each distal compartment $C1$–$C16$. The model cell's average discharge rate and average $C_\sigma(t)$ in the time interval $[60ms, 80ms]$ are 123.8 spikes/s and 0.41, respectively. This response pattern is again Chop-T.

ms. The resulting PSTHs for inhibitory input rates of 25 and 50 spikes/s (total discharge rate) are shown in Figs. 8A and 8B, respectively.

These data show that inhibition has a powerful effect on response of the model stellate cell despite the lack of any deterministic relationship between the times of occurrence of inhibitory and excitatory events. The chopping response seen subsequent to stimulus onset for the data of Fig. 7 is completely eliminated at inhibitory input rates of 25 spikes/s or greater, indicating that stochastic shunting inhibitory inputs applied to the distal dendritic region can effectively veto excitation in that region.

3.2.2 Effect of Stochastic Off-Path Shunting Inhibition At high stimulus levels, the selective process-

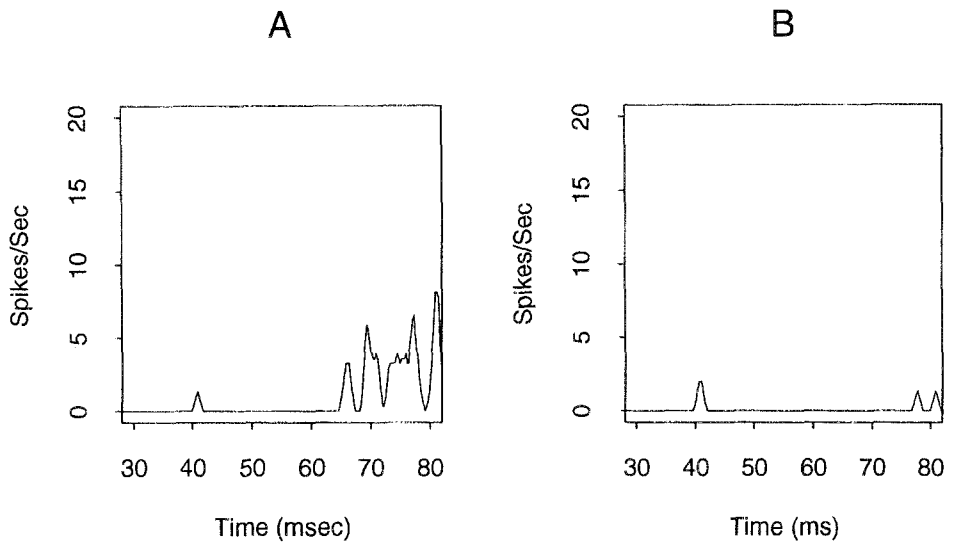

Fig. 8. The effect of on-path stochastic shunting inhibition, where one inhibitory input ($t_p^i = 1ms$) is applied to each distal compartment ($C1$–$C16$). The excitation pattern is the same as that of Fig. 7. Shown are PSTHs. The amplitude of the inhibitory conductance change is chosen to be $G_i = 80G_0$ (fixed for subsequent similar figures). The inhibition rates are 25 spikes/s (A) and 50 spikes/s (B). In both cases, on-path inhibitory inputs totally destroy the chopping response. When the inhibition rate is greater than 50 spikes/s, the model cell response is almost completely eliminated. Since the discharge rate of the inhibitory inputs decreases to a pleteau value after the onset of the stimulus, the inhibition is most effective at the beginning of the stimulus. This is the reason for a small number of spikes fired by the model cell towards the end of the stimulus.

ing hypothesis holds that stellate cell response is driven by synaptic inputs from high-threshold, low SR ANF's positioned on the proximal dendrite and/or soma. In this case, it is important to assess the influence of off-path shunting inhibitory inputs on response to proximal excitation. In order to do so, we uniformly distribute 8 low-medium SR ANF inputs in each proximal compartment and on the soma ($C17$–$C21$). This number is based on the observation by Liberman (1991) that stellate cells in the AVCNa (likely to be Chop-T cells; Bourk 1976) receive a larger number of low-medium SR fibers than high SR fibers in the proximal dendrite and on the soma with relative ratio being about 8:1. Since we use 1 high SR fiber in every distal compartment (Figs. 6 and 7), we use 8 low-medium fibers in every proximal compartment and on the soma.

Figures 9A–D show plots of PSTH (A), $\mu_{isi}(t)$ (B), $\sigma_{isi}(t)$ (C) and $c_\sigma(t)$ (D) for an input configuration where 8 low-medium SR ANF inputs with input rate of 100 spikes/s are applied to each of the compartments $C17$–$C21$. In this case, there is no excitatory input in the distal compartments $C1$–$C16$. The amplitude of the conductance change is $G_e = 6G_0$. The average discharge rate and the average $c_\sigma(t)$ value in the time interval $(60–80)ms$ are approximately 282 spikes/s and 0.258, respectively. Examination of the $\mu_{isi}(t)$, $\sigma_{isi}(t)$ and $c_\sigma(t)$ plots indicates that this chopping pattern is chop-S (Blackburn and Sachs 1989).

We next add one inhibitory input to each of the distal compartments $C1$–$C16$. Figures 10A-D show plots of PSTH (A), $\mu_{isi}(t)$ (B), $\sigma_{isi}(t)$ (C) and $c_\sigma(t)$ (D). Inhibitory rate is 50 spikes/s and t_p^i is $1ms$; parameter values leading to powerful inhibition based on the results of Sec. 2.2. The average discharge rate and average $c_\sigma(t)$ in $(60–80)ms$ are 172 spikes/s and 0.465, respectively. The response can be classified as chop-T (Blackburn and Sachs 1989). Comparison of Figs. 9A and 10A indicates that the chopping pattern is preserved in the presence of off-path inhibition, though both discharge rate and response regularity are decreased slightly (Banks and Sachs 1990). This observation is a general finding; chopping persists for inhibition rates as high as 100 spikes/s and t_p^i values as large as $2ms$. We conclude that for this particular placement of excitatory and inhibitory inputs, off-path shunting inhibition modeled by stochastic processes are ineffective in reducing somatic response to ANF inputs positioned proximally to (and on) the soma.

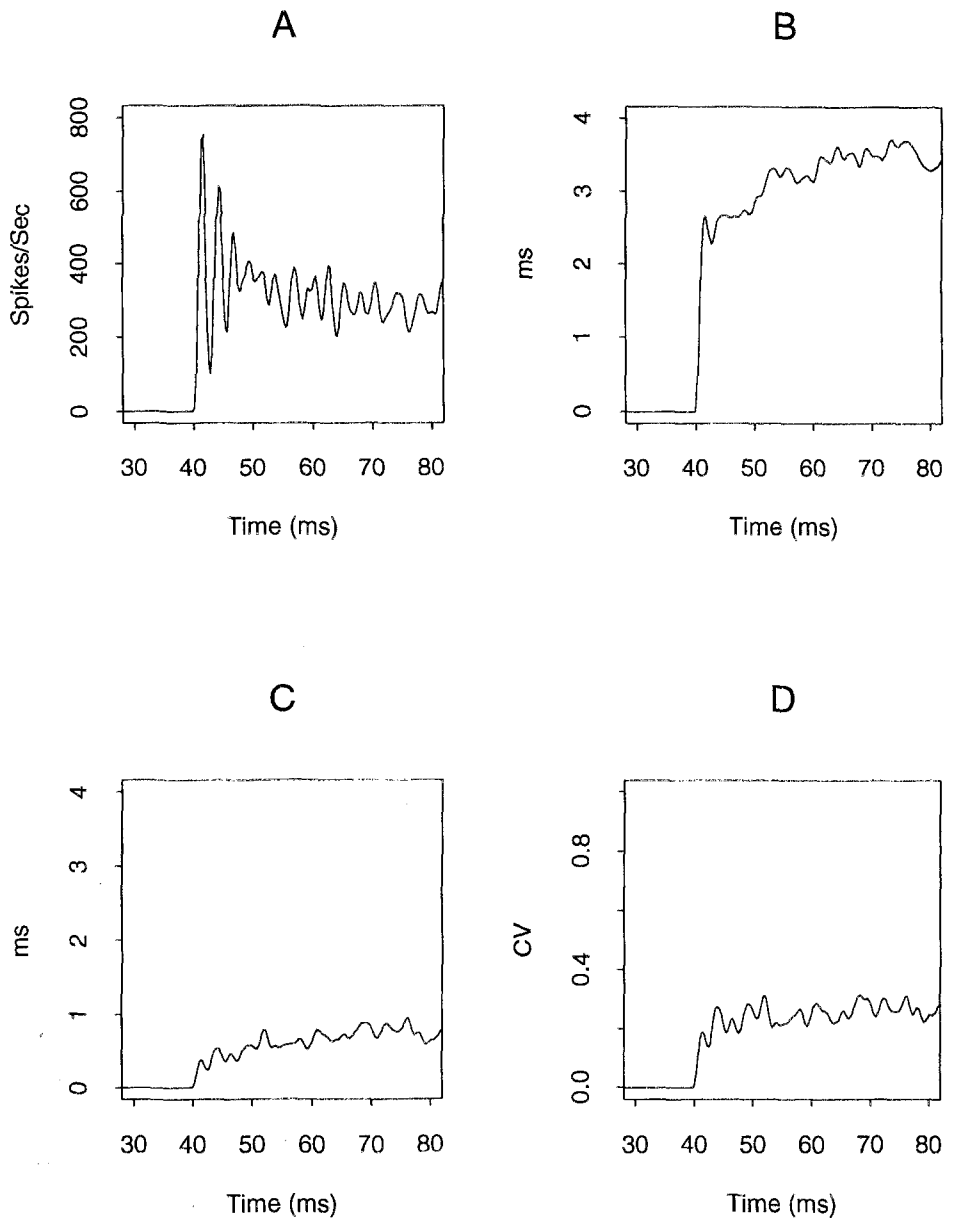

Fig. 9. Plots of PSTH (A), $\mu_{isi}(t)$ (B), $\sigma_{isi}(t)$ (C) and $C_\sigma(t)$ (D) when 8 low-medium SR fibers are applied to each of the proximal compartments and to the soma. The average discharge rate and average $C_\sigma(t)$ in the time interval [60*ms*, 80*ms*] are 282 spikes/s and 0.258, respectively. This response can be classified as Chop-S.

At high stimulus levels, the hypothesis holds that in addition to low-medium SR ANF and inhibitory inputs, there are also high SR ANF inputs firing at a saturating discharge rate in the distal dendritic region; synaptic currents generated by these inputs must be shunted. Figures 11A–D show the PSTH (A), $\mu_{isi}(t)$ (B), $\sigma_{isi}(t)$ (C), and $c_\sigma(t)$ (D) when one high SR ANF input is added to each distal compartment in addition to the low-medium ANF and inhibitory inputs in Fig. 10, modeling the situation at high stimulus levels. Both the inhibition rate and t_p^i are the same as in Fig. 10. The average discharge rate and average $c_\sigma(t)$ in (60–80)*ms* are 231 spikes/s and 0.383, respectively. This response can be classified as chop-T (Blackburn and Sachs, 1989). Note this models a cell which remains Chop-T at low and high stimulus levels. We

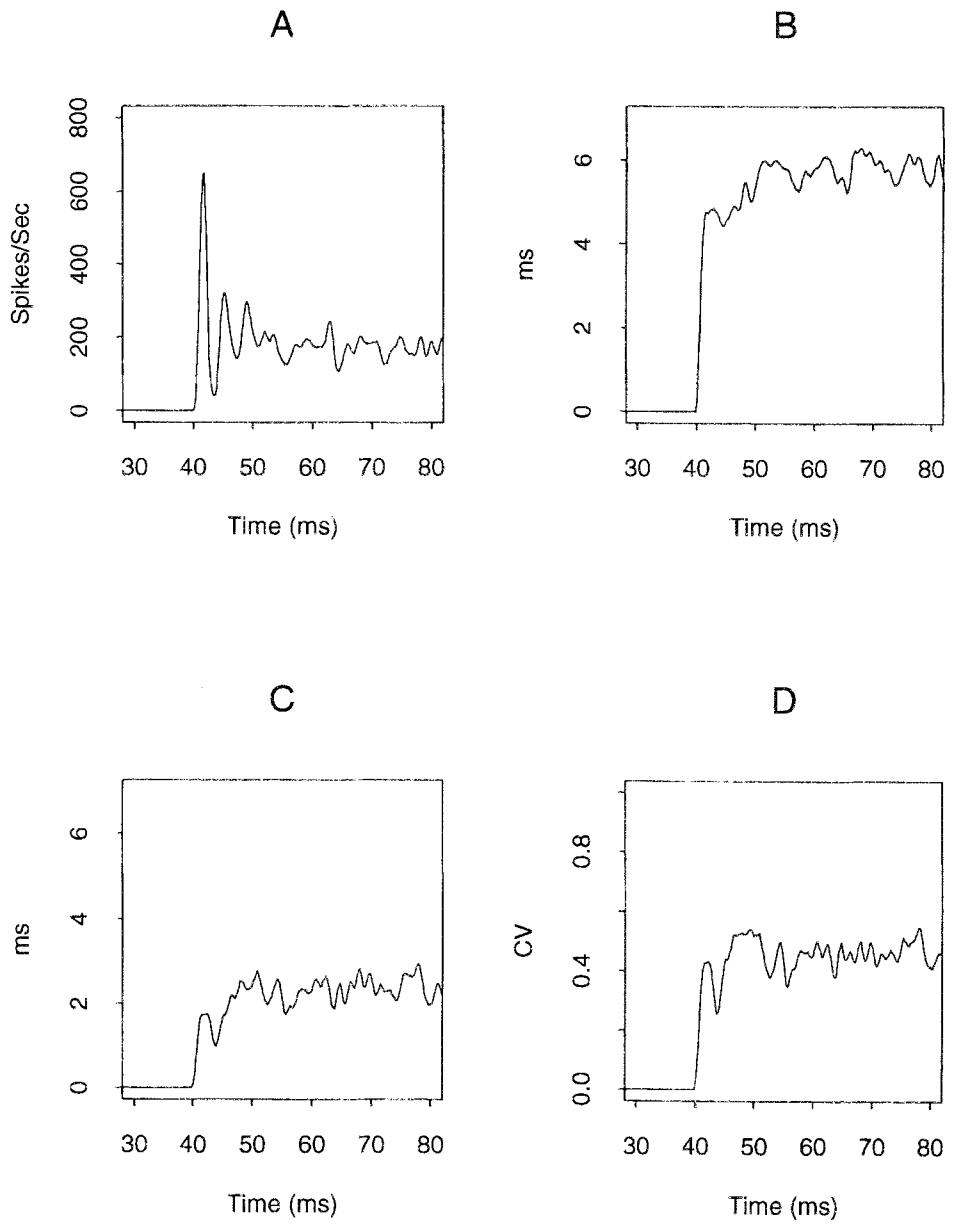

Fig. 10. Plots of PSTH (A), $\mu_{isi}(t)$ (B), $\sigma_{isi}(t)$ (C) and $C_\sigma(t)$ (D) when one inhibitory input (rate = 50 spikes/s, $t_p^i = 1ms$) is applied to each of the distal compartments $C1$–$C16$ besides the excitatory inputs in Fig. 9. The average discharge rate and the average $C_\sigma(t)$ are 172 spikes/s and 0.465, respectively. The response is Chop-T. In spite of the presence of distal inhibitory inputs, the chopping pattern of Fig. 9 still persists. This numerical experiment thus indicates that off-path stochastic inhibitory inputs only have a small effect to more proximal/somatic excitatory inputs.

have also tested several combinations of the inhibition rate and t_p^i, while holding the distribution of excitatory and inhibitory inputs constant. Table 2 shows the chopping type (whether Chop-S or Chop-T) for these different combinations (the symbol $*$ denotes marginal cases for which it is difficult to classify response as either Chop-T or Chop-S). The top row lists 4 different inhibition rates (in spikes/s), the leftmost column lists 4 different t_p^i's (in ms). The response of the cell is Chop-S when inhibition rate is 25 spikes/s and $t_P^i \leq 1ms$. This illustrates that a Chop-T cell at low stimulus levels (Fig. 7) can become a Chop-S cell

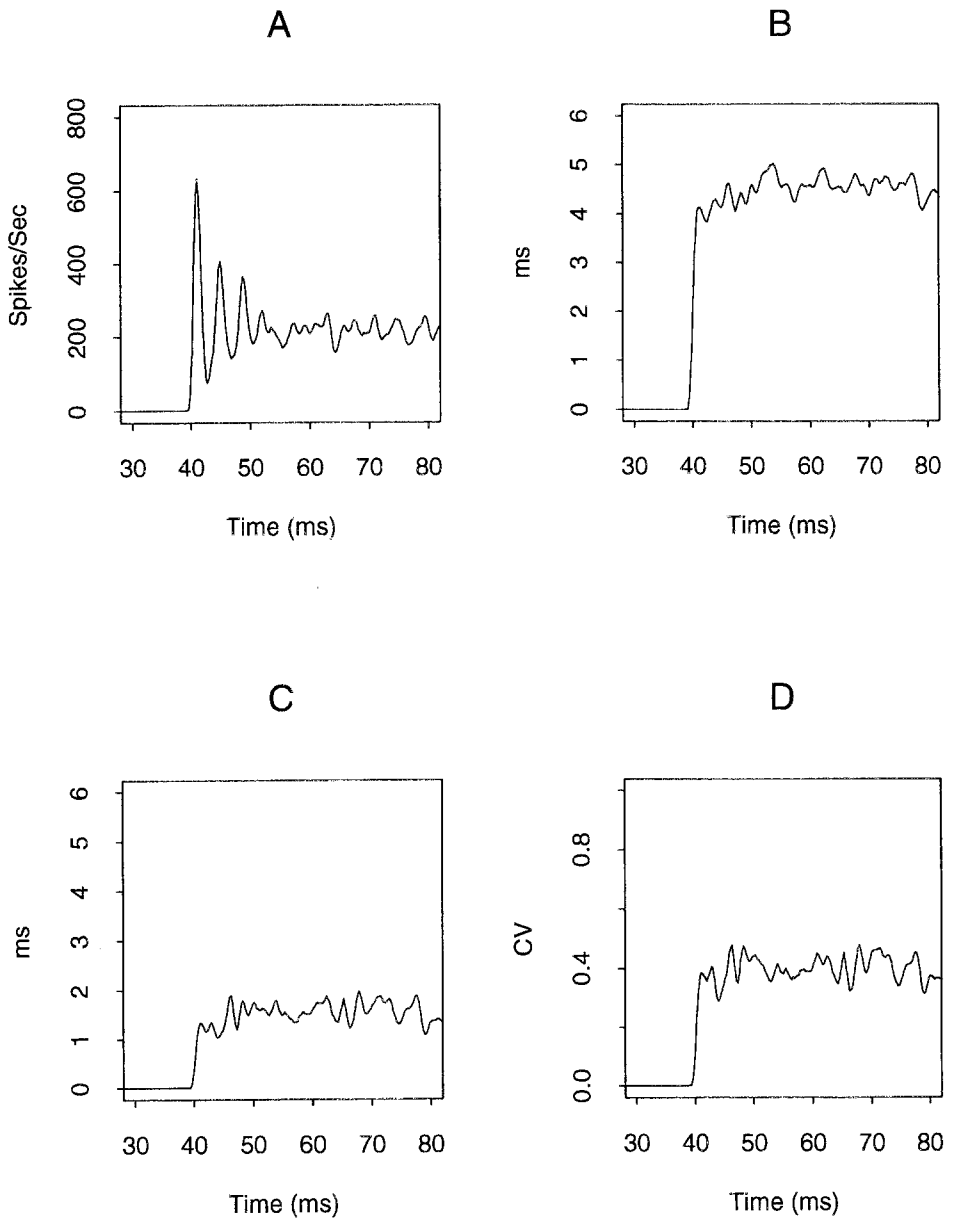

Fig. 11. Plots of PSTH (A), $\mu_{isi}(t)$ (B), $\sigma_{isi}(t)$ (C) and $C_\sigma(t)$ (D) when one high SR ANF input is applied to each distal compartment $C1$–$C16$ in addition to the inputs in Fig. 10. This input configuration simulates a possible innervation pattern of the stellate cell at high stimulus levels. The average discharge rate and average $C_\sigma(t)$ are 231 spikes/s and 0.383, respectively. This response can be classified as Chop-T. Note that due to the presence of high SR fibers in the distal compartments, model cell's average discharge rate is increased slightly (compared to 172 spikes/s in Fig. 10A).

at high stimulus levels at appropriate combinations of inhibition rate and t_p^i.

Note that steady-state discharge rate is increased in Fig. 11A as compared with Fig. 10A due to synaptic current generated by high SR ANF inputs in the distal region. Synaptic current generated by these distal inputs alone is not large enough to generate somatic action potentials (Fig. 8B). This current is large enough, however, to facilitate response to more proximal excitatory inputs (Fig. 11A) by producing a small depolarization of soma membrane potential. This is

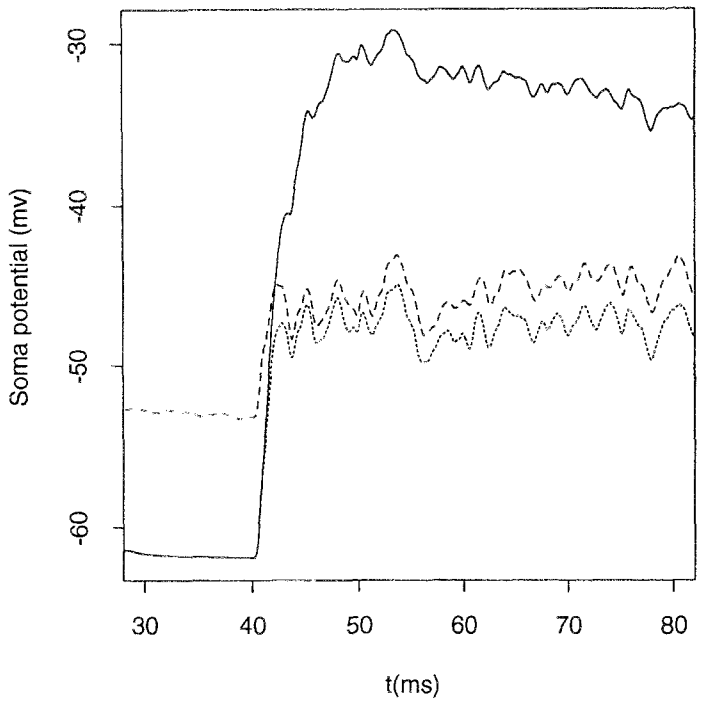

Fig. 12. Instantaneous passive soma voltage responses for the input configuration in Fig. 9 (solid line), Fig. 10 (dotted line) and Fig. 11 (dashed line). Off-path inhibition can reduce passive soma membrane potential (dotted line versus solid line). However, distal high SR fibers can produce current that facilitates response to more proximal/somatic excitatory inputs by producing a small depolarization of the soma potential (dashed line versus dotted line).

Table 2. Chopping response type (Chop-T or Chop-S) at 16 combinations of four inhibitory rates (the top row, in spikes/s) and four t_p^i's (the leftmost column, in *ms*), the time-to-peak of the inhibitory conductance change. The ANF and inhibitory input arrangement is the same as in Fig. 11 which mimic response of the "full" model at high stimulus levels (*e.g.*, input rate of the high SR ANFs is saturated). The criterion for determining whether a response is Chop-T or Chop-S is from Blackburn and Sachs (1989). The symbol *'s denote marginal cases.

	25	50	75	100
0.25	Chop-S	Chop-S	Chop-T*	Chop-S*
0.5	Chop-S	Chop-T	Chop-T	Chop-T
1.0	Chop-S	Chop-T	Chop-T	Chop-T
2.0	Chop-T	Chop-T	Chop-T	Chop-T

demonstrated in Fig. 12 which shows the soma membrane potential (averaged over 100 statistically independent trials) for the case of a passive soma for input configurations as in Fig. 9 (solid line; proximal excitatory inputs), Fig. 10 (dotted line; proximal excitatory inputs with off-path inhibition) and Fig. 11 (dashed line; proximal and distal excitatory inputs with distal inhibition).

3.2.3 A Summary of On-Path and Off-Path Stochastic Inhibition Figures 13A–B summarize our results for on- and off-path stochastic shunting inhibition. Figure 13A shows the ratio of discharge rate (R, plotted on the ordinate) when inhibition is present (1 input to each $C1$–$C16$) in the distal region to that when inhibition is absent. The upper four curves correspond to the off-path inhibition case (8 low SR ANF inputs to each $C17$–$C21$) and the four lower curves correspond to the on-path inhibition case (1 high SR ANF to $C1$–$C16$). The solid, dotted, short-dashed and long-dashed lines correspond to $t_p^i = 0.25ms, 0.5ms, 1ms$ and $2ms$, respectively. Figure 13B shows the same ratio versus t_p^i at different inhibition rates, where four upper (lower) curves correspond to the off-path (on-path) inhibition case and, the solid, dotted, short-dashed and long-dashed lines correspond to an inhibition rate of 25, 50, 75 and 100 spikes/s, respectively. As either the inhibition

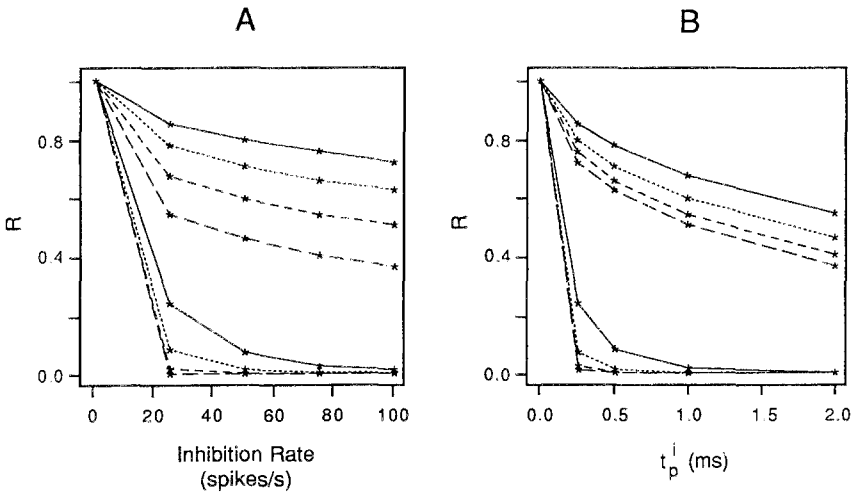

Fig. 13. A) Ratio R versus inhibition rate at different t_p^i values for on- (the lower four curves) and off-path (the upper four curves) cases as in Figs. 8 and 10, respectively. R is defined as the ratio of discharge rate with inhibition to that without inhibition. The solid, dotted, short-dashed and long-dashed curves correspond to t_p^i values of 0.25 *ms*, 0.5 *ms*, 1 *ms* and 2 *ms*, respectively. B) R versus t_p^i for inhibition rate of 25, 50, 75 and 100 spikes/s (solid, dotted, short-dashed and long-dashed curves, respectively). Those data show that on-path inhibitory inputs are highly effective to veto distal high SR ANF inptus, while off-path inhibitory inputs have only a small effect on proximal and somatic excitatory inputs. This is what is required for stellate cells to perform selective processing.

rate increases or t_p^i increases, on-path inhibition become increasingly effective ($R \rightarrow 0$). For off-path inhibition, R remains close to one for small values of t_p^i ($0.25ms$) or low inhibition rate (25 spikes/s). Even when t_p^i is $2ms$ and the inhibition rate is 100 spikes/s, R is still larger than 0.35. These data, together with Figs. 7–12, show a powerful effect of the on-path inhibition and the ineffectiveness of the off-path inhibition. This is precisely what is required for the stellate cell to perform selective processing.

4 Stellate Cell Responses to BF Tone Bursts of Varying Level

In this section, we simulate the response of a model stellate cell, with synaptic inputs arranged according to the selective processing hypothesis described in Sect. 1.3, to BF tones of varying level. The resulting model rate-versus-level functions (RVLFs) are then compared with those measured in cat AVCN stellate cells by Blackburn and Sachs (1990). Our goal is to determine whether or not the hypothesized stellate cell innervation pattern giving rise to selective processing can also reproduce RVLFs measured in cat AVCN stellate cells.

4.1 Peripheral Model

A first step in modelling AVCN stellate cell response to a BF tone of varying level is to simulate the response of primary ANFs with BF close to that of the stellate cell to the tone. It is also neccessary to model responses of the off-BF ANF fibers which will provide inhibitory inputs to the stellate cell through inhibitory interneurons.

We use a phenomenological model developed by Sachs and Abbas (1974) and Sachs et al. (1989) to simulate rate responses of ANFs to single tones of varying intensity. In this model, discharge rate R of ANFs in response to a tone at stimulus level P is given by

$$R = R_{sp} + R_D \frac{(D/\theta_E)^{1.77}}{1 + (D/\theta_E)^{1.77}}. \tag{4}$$

In Eq. (4), R_{sp} is the spontaneous rate (we choose 68 spikes/s for high SR ANFs and 0.5 spikes/s for low-medium SR ANFs, as in Sec. 3), R_D is the maximum driven rate (we choose 92 spikes/s for high SR ANFs and 100 spikes/s for low-medium SR ANFs), D is a quantity proportional to the basilar membrane displacement given by $D = P[\frac{1}{1+(P/\theta_I)^2}]^{0.33}$, where θ_I is a self-inhibitory threshold which is a constant for each auditory neuron. Let $\theta_{TC}(f)$ be the min-

imum stimulus level of a single tone of frequency f which evokes an increment in discharge rate above R_{sp}. Then θ_I can be determined from the tuning curve threshold at best frequency $\theta_{TC}(BF)$ by the following relationship (Sachs, Winslow and Sokolowski 1989),

$$\theta_I = \theta_{TC}(BF) + 30dB. \quad (5)$$

The only unknown parameter in Eqs. (4–5) is θ_E, which is the excitatory threshold that varies with the tone frequency f. θ_E is different for different group of on-BF and off-BF primary fibers. After θ_E is determined, RVLFs [the function R(P)'s] for high and low-medium SR on-BF ANFs and for off-BF fibers can then be calculated from Eqs. (4–5).

The procedure for calculating various θ_E's is as follows:

- For high SR ANFs at the same BF as the stellate cell, we choose $\theta_{TC}(BF) = 0$dB so that $\theta_I = 30$dB. The excitatory threshold θ_E is determined by solving Eq. (4) with $(R - R_{sp})/R_D = 0.05$ and $P = \theta_{TC} \times BF$. Thus, for a BF tone, the excitatory threshold is the sound pressure level producing a 5% increase in discharge rate above spontaneous rate.
- For low-medium SR ANFs at the same BF, θ_I is chosen to be $\theta_I = 30$dB, and θ_E is solved the same way as in the high SR ANF case except that we set $P = \theta_{TC}(BF) = 20$dB.

Model RVLFs for high and low-medium SR ANFs are shown in Fig. 14A as solid and dotted lines, respectively. Note that the RVLF of the low-medium SR ANF has a much wider dynamic range than that of the high SR ANF.

RVLFs for auditory-nerve fibers responding to off-BF tones were modeled as described by Neti and Young (1992). It is neccessary to treat below BF and above BF cases differently because RVLFs for above BF frequencies usually have lower slope values than those of below BF frequencies (Sachs and Abbas 1974). The following approach can be used to model RVLFs for both below and above BF fibers (Neti and Young 1992):

- For tone frequency $f < BF$, θ_E is chosen to be the same as that of on-BF high SR ANFs, but RVLF curves are parallel-shifted along the stimulus level axis according to the tuning curve. Specifically, the sound pressure variable P is replaced by $P - [\theta_{TC}(f) - \theta_{TC}(BF)]$ (in dB).
- For $f > BF$, θ_E is determined by solving Eq. (4) with $P = \theta_{TC}(f)$, and θ_I is still chosen to be 30dB. In this case, no shift along the stimulus axis is neccessary, so the rate is calculated with the actual sound pressure value.

As the stimulus level is increased, excitation will spread along the basilar membrane from the region of BF to nearby regions that correspond to different BFs. To model this spread of excitation in response to a single tone of frequency f at varying levels, it is neccessary to know the tuning curves for fibers at various BFs. While a large number of experimental tuning curves are available (*e.g.*, those measured by Delgutte), we use a simple extrapolation approach to systematically simulate tuning curves at various BFs. First, we pick a typical experimental tuning curve from the data base provided by Delgutte, say, at $BF = 8kHz$. Tuning curves at other BFs are approximated by shifting the tuning curve at $8kHz$ along the BF axis with values of $\theta_{TC}(BF)$ and $Q_{10}(BF)$ (the width of the tuning curve at stimulus level 10 dB above the threshold) taken from physiological measurements (Pickles 1988). Typically, ANF rate response thresholds increase linearly (on a logarithmic scale) when the tone frequency is varied from BF, with a much steeper slope on the above-BF side. To yield correct $Q_{10}(BF)$ values for tunning curves at different BFs, the below BF side of the tuning curve is adjusted. The functions $\theta_{TC}(BF)$ and $Q_{10}(BF)$ are experimentally available (Pickles 1988). From tuning curves at various BFs, the threshold $\theta_{TC}(f)$, where f is the tone frequency, can be extracted, and discharge rates at those BFs in response to a single tone of frequency f at various intensity levels can then be computed as described in the preceding paragraph. Figure 14B shows a model plot of spread of excitation along the basilar membrane in response to a tone of $5.5kHz$ at 20dB, 30dB, 40dB, 60dB, 80dB and 100dB, where the ordinate is normalized rate and the abscissa denotes the BF. Note the asymmetric spread of activation to higher frequency regions with increasing stimulus levels. RVLFs for off-BF fibers are easily calculated using the data from Fig. 14B. Discharge rates as a function of stimulus level for an off-BF fiber at the f_1 kHz place can be obtained from curves corresponding to different stimulus levels in Fig. 14B at the frequency f_1.

In the following model, stellate cell BF is set to $5.5kHz$. Inhibition (through interneurons) is gener-

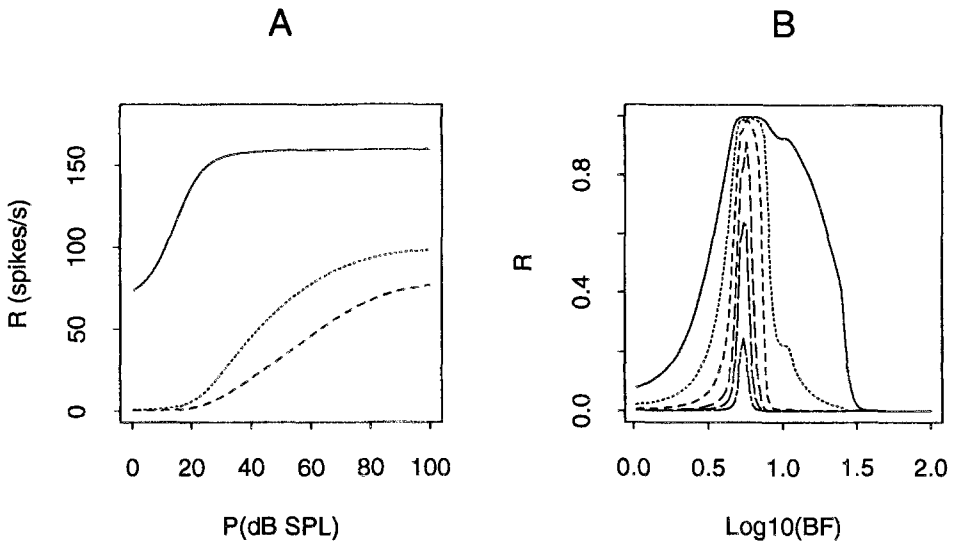

Fig. 14. A) Rate-versus-level functions for a low-threshold, high SR fiber (solid line), a high-threshold, low-medium SR fiber (dotted line) at $BF = 5.5kHz$ and a high SR fiber at $BF = 6.6kHz$ (dashed line). The abscissa plots sound pressure levels in dB SPL. The ordinate denotes the discharge rate. These RVLFs are obtained using a peripheral model similar to that proposed by Sachs and Abbas (1974). See text for details. B) Spread of excitation along the basilar membrane calculated using the same model. The abscissa denotes the best frequency on a logarithmic scale. The ordinate is a normalized rate. Six curves denote the basilar membrane response to a tone of 5.5 kHz at 20 dB, 30 dB, 40 dB, 60 dB, 80 dB and 100 dB, respectively. The above BF RVLF in the Panel A (dashed line) corresponds to a fiber with BF at roughly 6.6kHz. RVLF for this above-BF fiber is calculated by reading off the discharge rate at 6.6kHz from curves in the Panel B at different stimulus levels.

ated by responses of model ANFs with BF at $6.6kHz$ whose RVLF is shown in Fig. 14A (dashed line). This choice of frequency is based on a stellate cell receptive field plot measured by Blackburn and Sachs (1992; Fig. 5). Since nothing is known regarding the nature of the inhibitory interneuron, we have made the simplest possible assumption that interneurons fire in a one-to-one fashion in response to ANF inputs. Two inhibitory inputs were applied to each distal compartment. This choice is arbitrary, since nothing is known regarding the precise innervation of the distal inputs.

4.2 Rate-Versus-Level Functions for Stellate Cells

Stellate cell RVLFs were generated by computing discharge rate to BF tones with level ranging from 0 to 100 dB SPL in steps of 2 dB. For each stimulus level, rates for high SR ANF, low-medium SR ANF and inhibitory inputs are chosen according to Fig. 14A. Based on these rates, ANF and inhibitory spike trains are produced using the method described in Sec. 3.1. These spike trains serve as the input to the stellate cell. The model stellate cell receives 1 high SR ANF input and 1 shunting inhibitory input in each distal compartment, and 8 low-medium SR ANF inputs in each proximal compartment and on the soma. As in Sec. 3, the excitatory and inhibitory conductances are chosen to be $G_e = 6G_0$ and $G_i = 80G_0$, respectively. Time-to-peak of the inhibitory conductance change is $t_p^i = 0.25ms$. The output discharge rates of the stellate cell at each stimulus level are computed using 50 statistically independent input spike trains. Stellate cell RVLFs are obtained by plotting these output rates against the stimulus level. A 5-point moving triangular window is used to smooth the RVLFs.

Experimentally measured stellate cell discharge rate increases rapidly when stimulus level is increased from 0dB to 25dB (Blackburn and Sachs 1990). This range of about 25dB is consistent with the dynamic range of high SR ANFs (Fig. 14A, solid line). After this initial increase, as the stimulus level is increased further, stellate cell RVLFs exhibit one of three behaviors (Blackburn and Sachs 1990): (1) discharge rate increases slowly; (2) discharge rate remains at a plateau value; and (3) discharge rate decreases slowly.

The relative size of the distal and proximal dendritic regions is an important parameter when modeling these RVLFs. Figures 15A–C show three types of stellate cell RVLFs computed from our model using

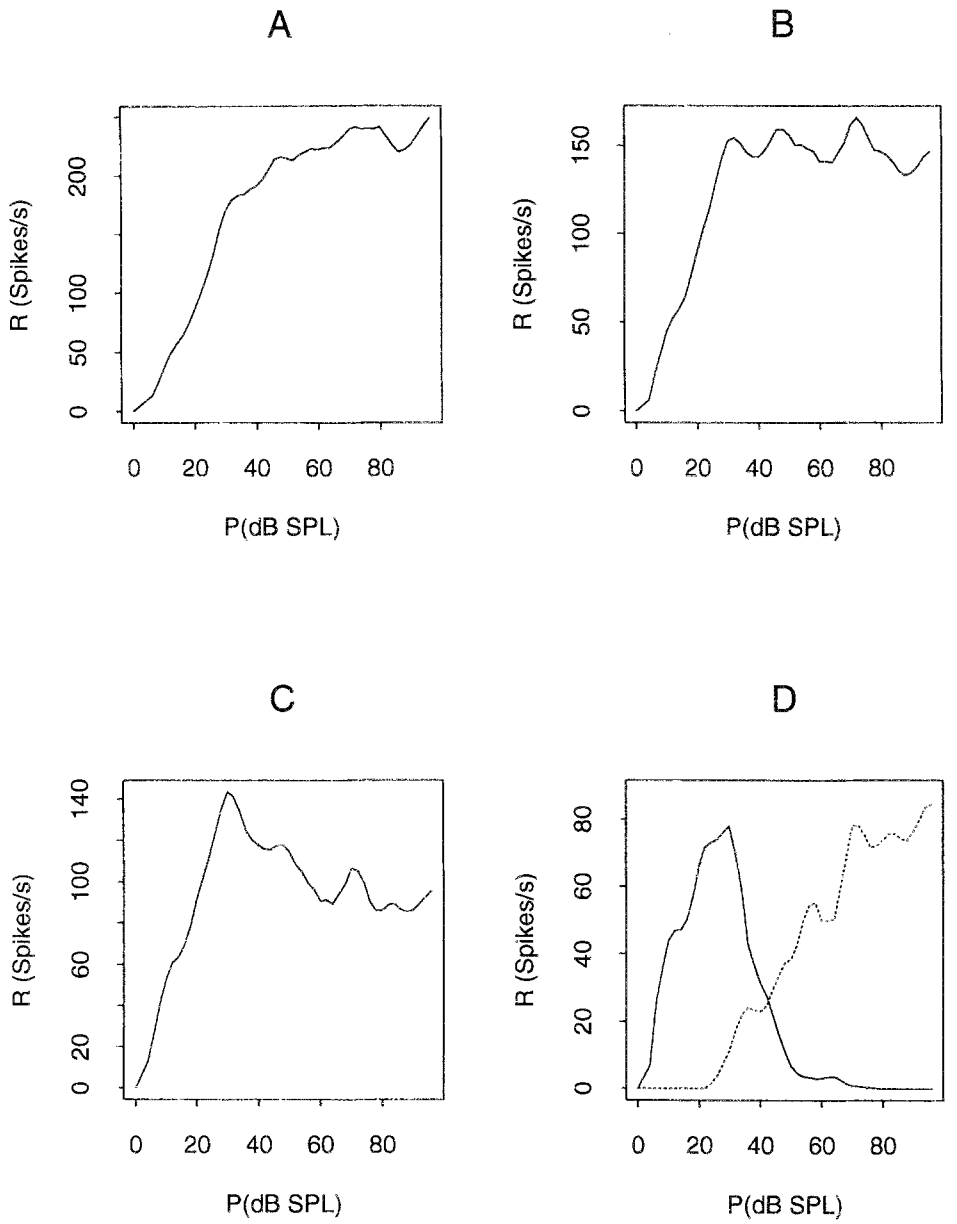

Fig. 15. Three types of model stellate cell RVLFs when excitatory inputs from ANFs and inhibitory inputs are arranged according to the selective processing hypothesis. Input configurations are similar to that of Fig. 11. RVLFs for primary fibers and for inhibitory inputs are taken from Fig. 14A. A–C) Three panels corresponding to relative sizes of the distal and proximal dendritic region of 0.8 : 0.2, 0.9 : 0.1 and 0.95 : 0.05, respectively. D) RVLFs for two cases where there are only high SR fibers in the distal region (the solid line) and only low-medium SR fibers in the proximal region (the dotted line). The relative size of the distal and proximal regions is 0.9 : 0.1, and inhibition is present in the distal region for both curves. Nonlinear interaction of the distal, proximal excitation and inhibition gives the RVLF in (B). Panel (D) thus demonstrates that the main contribution to stellate cell RVLF is distal high SR fibers at low stimulus levels and proximal low-medium SR fibers at high stimulus levels.

the following relative sizes: 0.8 : 0.2 (A), 0.9 : 0.1 (B) and 0.95 : 0.05 (C). In all three plots, the initial rapid increase in discharge rate occurs over the initial 25dB range of input levels. This rapid increase in discharge rate at stimulus levels just above threshold is due to inputs from high SR ANFs in the distal region. For stimulus levels > 25dB, both low-medium SR ANF and inhibitory input rates begin to

increase. As stimulus level is increased, on-path inhibitory inputs veto high SR ANF inputs in the distal region. Hence, when stimulus level is greater than about 30dB, the main synaptic inputs which drive the stellate cell are from low-medium SR ANFs in the proximal region. Figure 15D shows RVLFs for the case where inhibitory inputs are applied distally, and where there are either distal excitatory inputs from high SR ANFs (solid line), or proximal/somatic inputs from low-medium SR fibers (dotted line). The relative size of the distal and proximal regions are identical to that in Fig. 15B. At low stimulus levels, excitation from high SR ANFs drives the model stellate cell. However, as stimulus levels increase, excitatory synaptic current generated by these inputs is shunted by the inhibitory inputs (solid line). At these high stimulus levels, the more proximal/somatic inputs from low-medium SR fibers drive the model cell. This is precisely the behavior required for selective processing.

Since off-path inhibition does have some effect (Fig. 13), the extent to which low-medium SR ANF inputs drive the stellate cell is determined by the relative size of the distal inhibitory region and the proximal excitatory region. The larger the distal region is, the greater the observed reduction of the discharge rate. In Fig. 15A, the size of the distal region is relatively small. This causes a slow increase in the discharge rate due to a continuous increase in the input rate of low-medium SR ANFs as the stimulus level is increased. In Fig. 15B, the distal region is larger. In this case, the effect of off-path inhibition just balances the increase in the low-medium SR ANF input rate, giving rise to a plateau in the discharge rate of the stellate cell. In Fig. 15C, the distal region is relatively large. In this case, the effect of off-path inhibition is strong, leading to a slow decrease in the stellate cell discharge rate in spite of a steady increase in the low-medium SR ANF input rate. The non-monotonic RVLF in Fig. 15C is the most commonly observed type in real stellate cells (Blackburn and Sachs 1990).

When inhibition characteristics (*e.g.*, G_i and t_p^i) are changed, RVLF from the model stellate cell also changes. However, the monotonic and non-monotonic behaviors (Fig. 15) can still be reproduced by choosing different relative sizes of the distal and proximal dendritic regions. We henceforth speculate that the relative size of the innervation regions for excitatory and inhibitory inputs may crucially determine the response characteristics of stellate cells.

5 Discussion

The data of Blackburn and Sachs (1990) show that AVCN stellate cells maintain a robust rate-place representation of vowel spectra over a wide range of stimulus levels. This rate-place representation resembles that of low threshold, high SR auditory nerve fibers *at low stimulus levels*, and that of high threshold, low-medium SR ANFs *at high stimulus levels*. One hypothesis (Winslow et al. 1987) accounting for these data is that AVCN stellate cells selectively process inputs from different SR population of ANFs in a level-dependent fashion. We have formulated a model of AVCN stellate cells. Using this model, we have shown that spatial segregation of excitatory inputs from low and high threshold ANFs as well as input from inhibitory interneurons within the stellate cell dendritic tree can give rise to selective processing. The model successfully reproduces various experimentally observed PSTHs and RVLFs for stellate cells. We stress, however, that the present model deals with selective processing of ANF inputs by stellate cells in response to single tones. To reproduce response properties of stellate cells to more complicated sound stimulus such as vowels, a network model of stellate cells with each cell performing selective processing at a unique frequency is required. Nonetheless, the present work represents a first step towards the development of a computational model of the AVCN stellate cell receptive field.

The majority of BF tone rate-level functions measured from cat AVCN stellate cells are non-monotonic at high stimulus levels. These non-monotonic rate-level functions can be reproduced by the model (Fig. 15). In terms of the model, non-monotonic behavior reflects the influence of distal inhibitory inputs on more proximal excitatory inputs from low-medium SR ANFs. Clearly, non-monotonic rate responses are of little value for discriminating changes in tone intensity; there are sound levels at which intensity increments cannot be detected as being different from intensity decrements. The importance of these responses lies in the fact that at higher stimulus levels (levels greater than about 30 dB SPL for the model stellate cell in Fig. 15D), responses are determined solely by inputs from low-medium SR ANFs. As a

result, non-monotonicity of RVLFs reflects the ability of stellate cells to encode the spectral envelope of broadband acoustic signals at very high stimulus levels, as observed by Blackburn and Sachs (1990).

There is morphological evidence of non-cochlear somatic inhibitory inputs to AVCN stellate cells (Type II cells in particular, Cant 1981). The source of these inputs is unknown; they could be inputs from either CN interneurons, or from descending efferent fibers. Our model does not include direct somatic inhibition. Instead, somatic inhibition is mediated by electrotonic influences of inhibitory inputs to the distal dendritic region closest to the soma. Direct somatic inhibitory inputs would not prevent our model from functioning as we have described as long as inhibition is comparable in magnitude to that resulting from the electrotonic influences studied here. Powerful somatic inhibition driven indirectly by off-BF ANF activity would eliminate stellate cell response at high stimulus level. This would produce model stellate cell RVLFs with very strong non-monotonic behavior; behavior which is not observed physiologically.

There are other possible mechanisms for selective processing which we have not yet investigated. For example, selective processing may result from the existence of voltage-gated conductances in the stellate cell distal dendrites which are activated following depolarization of cell membrane potential. These conductances would be minimally activated at low stimulus levels since at these levels, the mean depolarization generated by high SR ANF synaptic inputs is low. At high stimulus levels, the saturating response of high SR ANF inputs would produce an increase of the mean depolarization level. This could in turn activate potassium conductances and prevent synaptic current from flowing to the soma. While this selective processing mechanism is possible, at present there is no evidence that supports the existence of such voltage-gated conductances in the stellate cell dendrites. Nor is there any failure of our model that necessitates the incorporation of active dendritic channels. Voltage-dependent processes in dendrites may play important functional role in other neurons. Softky and Koch (1992, 1993) have speculated that active processes may be responsible for the highly irregular firing pattern observed in cortical cells of awake macaque monkey responding to visual stimuli. These cells receive a large number of small amplitude synaptic inputs on their dendrites and, therefore, would fire with high regularity if there were no voltage-dependent processes present in dendrites (Softky and Koch 1992; Softky and Koch 1993). There is no such discrepancy between the extent of dendritic integration and discharge regularity in the model presented here. However, if morphological studies demonstrate that there are in fact large numbers of ANF inputs to stellate cell dendrites, then the passive model described here would also produce highly regular discharges and could not account for CV values observed in real stellate cells. In such a case, dendritic active channels might be required to account for irregularly firing stellate cell responses.

A second alternative model, which is a slight modification of the model proposed here, must be considered. In this model, inhibitory interneurons projecting to the distal region of the stellate cell dendritic tree receive inputs from on-BF, high threshold fibers rather than off-BF fibers. With appropriate spatial arrangement of high SR, low-medium SR fibers and inhibitory inputs, this scheme could also give rise to selective processing. We cannot as yet rule out this model. However, due to high response threshold of low SR fibers, it seems that this scheme would require very high stimulus level for off-BF inhibitory inputs to be fully activated. This may in turn produce model receptive field plots with inhibitory sidebands significantly shifted to high stimulus levels. This issue can only be addressed by calculation of response maps for the two model so that they may be compared to those measured experimentally.

It is commonly believed that the origin of the chopping responses of stellate cells are a combined effect of the passive filtering property of stellate cell dendrites and summation of small amplitude EPSPs in order to reach threshold (Young et al. 1988; Blackburn and Sachs 1989). Our model suggests the following hypothesis regarding the origin of Chop-T and Chop-S responses. Chop-S cells exhibit maintained chopping responses, and do not have an initial adaptation period during which the coefficient of variation increase significantly. Chop-S cell responses (Fig. 9) may therefore be influenced heavily by inputs from low-medium SR ANFs, since these fibers exhibit significantly less rate adaptation than do high SR fibers (Figs. 5A–B). Chop-T cells exhibit the highest degree of regularity near stimulus onset (see Fig. 7). This suggests that Chop-T cell responses may be more heavily influenced by high SR ANF inputs, because responses of these fibers have stronger rate adaptation at stimulus onset than do low-medium SR fibers. Also

note that in Figs. 6 and 7 we have demonstrated model Chop-T responses without applying any inhibitory input. This is an exception to previous modeling results (Banks and Sachs 1991) in which Chop-T responses were produced as a result of spatio-temporal patterning of inhibitory inputs.

Morphologically, there are two types of stellate cells (Cant 1981; Liberman 1991). Type II cells receive much greater innervation on the soma than do Type I cells. Physiologically, stellate cells can be classified into two major groups: Chop-T and Chop-S cells. While there seems to exist a correspondence between morphologically distinguished Type I and Type II and physiologically distinguished Chop-T and Chop-S stellate cells, respectively (Banks and Sachs 1991), our numerical results suggest that a model stellate cell may change its chopping characteristics as a function of stimulus level. This can be seen by Fig. 7, Fig. 11 and Table 2. With synaptic inputs arranged according to the selective processing hypothesis, at low stimulus levels, the model response can be Chop-T (Fig. 7). At high stimulus levels, depending on the inhibition rate and t_p^i, the model response can be either Chop-T (for example, Fig. 11) or Chop-S (Table 2). Therefore, at present there is no assurance that morphologically different stellate cells would correspond to physiologically different chopping patterns, since chopping pattern may depend on stimulus level. In fact, studies by Smith and Rhode (1989) of onset choppers in the anterior posteroventral cochlear nucleus (A-PVCN)/nerve root region indicate that Chop-T responses at low stimulus levels may become more like Chop-S response at high stimulus levels (Fig. 2, Smith and Rhode 1989).

Finally, three important parameters that determine the dynamic characteristics of stellate cells have been identified. First, the inhibitory conductance change G_i, must be much larger than the excitatory conductance change G_e in order to achieve a powerful inhibition required for selective processing. Second, the time to peak of the inhibitory conductance change, t_p^i, is a sensitive parameter that determines the effectiveness of inhibition in selective processing. We have used values for t_p^i in a range $[0, 2]ms$. This parameter, combined with the rate of inhibition, critically determines PSTHs and chopping types of stellate cells at high stimulus levels. Therefore, a precise estimate of t_p^i should be obtained. Third, the relative ratio of the distal and proximal dendritic regions determines the characteristics of RVLFs for stellate cells, *i.e.*, whether monotonic or non-monotonic.

Acknowledgement

We thank E. D. Young for many valuable discussions. We are also grateful for the ANF tuning curves provided by B. Delgutte. This work was supported by the ONR Grant # N00014-92-J-1134 and by the NIH Grant #$DC00979 - 03$.

References

Adams, J. C. 1983. Multipolar cells in the ventral cochlear nucleus project to the dorsal cochlear nucleus and the inferior colliculus. Neurosci. Lett., 37:205–208.

Adams, J. C. and Warr, W. B. 1976. Origins of axons in the cat's acoustic striae determined by injection of horseradish peroxidase into several tracts. J. Comp. Neurol., 170:107–121.

Banks, M. I. and Sachs, M. B. 1991. Regularity analysis in a compartmental model of chopper units in the anteroventral cochlear nucleus. J. Neurophysiol., 65(3):606–629.

Barta, P. E. and Young, E. D. 1986. Rate responses of auditory nerve fibers to tones in noise near masked threshold. J. Acoust. Soc. Am., 79:426–442.

Berglund, A. M., Jacob, K., and Liberman, M. 1993. Morphometry of synaptic vesicles in anteroventral cochlear nucleus: Some correlations with terminal origins. In 16th Midwinter Research Meeting, Association for Research in Otolaryngology, St. Petersburg Beach, FA.

Blackburn, C. C. and Sachs, M. B. 1989. Classification of unit types in the anteroventral cochlear nucleus: PST histograms and regularity analysis. J. Neurophysiol., 62(6):1303–1329.

Blackburn, C. C. and Sachs, M. B. 1990. The representations of the steady-state vowel sound /e/ in the discharge pattern of cat anteroventral cochlear nucleus neurons. J. Neurophysiol., 63(5):1191–1212.

Blackburn, C. C. and Sachs, M. B. 1992. Effects of off-bf tones on responses of chopper units in ventral cochlear nucleus i. regularity and temporal adaptation patterns. J. Neurophysiol., 68(1):124–143.

Bourk, T. R. 1976. Electrical responses of neural units in the anteroventral cochlear nucleus of the cat. PhD thesis, Massachusetts Institute of Technology. Cambridge, MA.

Cant, N. B. 1981. The fine structure of two types of stellate cells in the anterior division of the anteroventral cochlear nucleus of the cat. Neuroscience, 6:2643–2655.

Cant, N. B. and Morest, D. K. 1978. Axons from non-cochlear sources in the anteroventral cochlear nucleus of the cat: A study with the rapid golgi method. Neuroscience, 3:1003–1029.

Cant, N. B. and Morest, D. K. 1979. Organization oe the neurons in the anterior division of the anteroventral cochlear nucleus of the cat: Light microscopic observations. Neuroscience, 4:1909–1923.

Costalupes, J. A. 1985. Representation of tones in noise in the responses of auditory nerve fibers in cats: I. comparison with detection threshold. J. Neurosci., 5:3261–3269.

Fekete, D. M., Rouiller, E. M., Liberman, M. C., and Ryugo, D. K. 1982. The central projections of intracellularly labeled auditory nerve fibers in cats. J. Comp. Neurol., 229:432–450.

Gaumond, R. P., Molnar, C. E., and Kim, D. O. 1982. Stimulus and recovery dependence of cat cochlear nerve fiber spike discharge probability. J. Neurophysiol., 48:856–873.

Johnson, D. and Kiang, N. Y. S. 1976. Analysis of discharges recorded simultaneously from pairs of auditory nerve fibers. Biophys. J, 16:719–734.

Johnson, D. H. and Swami, A. 1983. The transmission of signals by auditory-nerve fiber discharge patterns. J. Acoust. Soc. Am., 74:493–501.

Kiang, N. Y. S. and Moxon, E. C. 1974. Tails of tuning curves of auditory nerve fibers. J. Acoust. Soc. Am., 55:620–630.

Koch, C. and Poggio, T. 1986. Biophysics of computation: Neurons, synapses, and membranes. In Edelman, G. E., Gall, W. E., and Cowan, W. M., editors, Synaptic Function, New York. John Wiley & Sons.

Koch, C., Poggio, T., and Torre, V. 1982. Retinal ganglion cells: A functional interpretation of dendritic morphology. Phil. Trans. R. Soc. Lond. B, 227:227–264.

Li, J. 1991. Estimation of the recovery of discharge probability in cat auditory-nerve spike trains and computer simulations. PhD thesis, The Johns Hopkins University, Department of Biomedical Engineering. Baltimore, MD.

Liberman, M. C. 1991. Central projections of auditory-nerve fibers of differing spontaneous rate. i. anteroventral cochlear nucleus. J. Comp. Neurol., 313:240–258.

Lorente de No, R. 1981. The Primary Acoustic Nuclei. Raven, New York.

Manis, P. B. and Marx, S. O. 1991. Outward currents in isolated ventral cochlear nucleus neurons. J. Neurosci., 11(9): 2865–2880.

Merzenich, M. M., Knight, P. L., and Roth, G. L. 1975. Representation of the cochlea within primary auditory cortex in the cat. J. Neurophysiol., 38:231–249.

Neti, C. and Young, E. D. 1992. Neural network models of sound localization based on directional filtering by the pinna. J. Acoust. Soc. Am., 92(6):3140–3156.

Oertel, D. 1983. Synaptic responses and electrical properties of cells in brain slices of the mouse anteroventral cochlear nucleus. J. Neurosci., 3:2043–2053.

Oertel, D., Wu, S. H., and Hirsch, J. A. 1988. Electrical characteristics of cells and neuronal circuitry in the cochlear nuclei studied with intracellular recording from brain slices. In Edelman, G. M., Gall, W. E., and Cowan, W. M., editors, Auditory Function, New York. Wiley.

Osen, K. K. 1969. Cytoarchitecture of the cochlear nuclei in the cat. J. Comp. Neurol., 136:453–484.

Osen, K. K. 1970. Course and termination of the primary afferents in the cochlear nuclei of the cat: An experimental study. Arch. Ital. Biol., 108:21–51.

Pickles, J. O. 1988. An Introduction to the Physiology of Hearing. Academic Press, London.

Rall, W. 1964. Theoretical significance of dendritic trees for neuronal input-output relations. In Reiss, R. F., editor, Neural Theory and Modeling, pages 73–97, Stanford, CA. Stanford University Press.

Rall, W. 1977. Core conductor theory and cable properties of neurons. In Handbook of Physiology: The Nervous System. Cellular Biology of Neurons, volume 1, chapter 3, pages 39–97. Am. Physiol. Soc., Bethesda, MD.

Rhode, W. S., Oertel, D., and Smith, P. H. 1983. Physiological response properties of cells labeled intracellularly with horseradish peroxidase in the cat ventral cochlear nucleus. J. Comp. Neurol., 213:448–463.

Rothman, J. S. 1991. An electrophysiological model of bushy cells of the anteroventral cochlear nucleus. Master's thesis, The Johns Hopkins University, Department of Biomedical Engineering. Baltimore, MD.

Rouiller, E. M., Cronin-Schreiber, R., Fekete, D. M., and Ryugo, D. K. 1986. The central projections of intracellularly labeled auditory nerve fibers in the cat: An analysis of terminal morphology. J. Comp. Neurol., 249:261–278.

Rouiller, E. M. and Ryugo, D. K. 1984. Intracellular marking of physiologically characterized cells in the ventral cochlear nucleus of the cat. J. Comp. Neurol., 225:167–186.

Ryugo, D. K. and Rouiller, E. M. 1988. Central projections of intracellularly labeled auditory nerve fibers in cats: Morphometric correlations with physiological properties. J. Comp. Neurol., 271:130–142.

Ryugo, D. K., Wright, D. D., and Pongstaporn, T. 1993. Ultrastructural analysis of synaptic endings of auditory nerve fibers in cats: Correlations with spontaneous discharge rate. In Merchan, M., Juiz, J. M., Godfrey, D. A., and Mugnaini, E., editors, The Mammalian Cochlear Nuclei: Organization and Function, pages 65–74. Plenum Press.

Sachs, M. B. and Abbas, P. J. 1974. Rate versus level functions for auditory-nerve fibers in cats: tone-burst stimuli. J. Acoust. Soc. Am., 56:1835–1847.

Sachs, M. B., Winslow, R. L., and Sokolowski, B. H. A. 1989. A computational model for rate-level functions from cat auditory-nerve fibers. Hearing Res., 41:61–70.

Sachs, M. B. and Young, E. D. 1979. Encoding of steady-state vowels in the auditory-nerve: Representation in terms of discharge rate. J. Acoust. Soc. Am., 66:470–479.

Shofner, W. P. and Sachs, M. B. 1986. Representation of a low-frequency tone in the discharge rate of populations of auditory-nerve fibers. Hearing Res., 21:91–95.

Shofner, W. P. and Young, E. D. 1985. Excitatory/inhibitory response types in the cochlear nucleus: Relationships to discharge patterns and responses to electrical stimulation of the auditory nerve. J. Neurophysiol., 54(4):917–939.

Smith, P. H. and Rhode, W. S. 1989. Structural and functional properties distinguish two types of multipolar cells in the ventral cochlear nucleus. J. Comparative Neurology, 282:595-616.

Softky, W. R. and Koch, C. 1992. Cortical cells should fire regularly, but do not. Neural Computation, 4:643–646.

Softky, W. R. and Koch, C. 1993. The highly irregular firing of cortical cells is inconsistent with temporal integration of random epsps. J. Neuroscience, 13:334–350.

Wang, X. 1991. Neural encoding of single-formant stimuli in auditory-nerve and anteroventral cochlear nucleus of the cat. PhD thesis, The Johns Hopkins University, Department of Biomedical Engineering. Baltimore, MD.

White, J. A. 1990. Electrotonic models of stellate cells of the ventral cochlear nucleus. PhD thesis, The Johns Hopkins University, Department of Biomedical Engineering. Baltimore, MD.

Winslow, R. L., Barta, P. E., and Sachs, M. B. 1987. Rate coding in the auditory nerve. In Watson, C. S. and Yost, W., editors, Auditory Processing of Complex Sounds, pages 212–224. Lawrence Erlbaum Associates.

Wu, S. H. and Oertel, D. 1984. Intracellular injection with horseradish peroxidase of physiologically characterized stellate and bushy cells in slices of mouse anteroventral cochlear nucleus. J. Neurosci., 4:1577–1588.

Wu, S. H. and Oertel, D. 1986. Inhibitory circuitry in the ventral cochlear nucleus is probably mediated by glycine. J. Neurosci., 6:2691–2706.

Young, E. and Sachs, M. B. 1979. Representation of steady-state vowels in the temporal aspects of the discharge patterns of populations of auditory-nerve fibers. J. Acoust. Soc. Am., 66:1381–1403.

Young, E. D., Robert, J. M., and Shofner, W. P. 1988a. Regularity and latency of units in the ventral cochlear nucleus: Implications for unit classification and generation of response properties. J. Neurophysiol., 60:1–29.

Young, E. D. and Sachs, M. B. 1988. Interactions of auditory nerve fibers and ventral cochlear nucleus cells studied with cross-correlation. In 18th Annual Meeting, Society for Neuroscience Abstracts, Toronto, Canada.

Young, E. D., Shofner, W. P., White, J. A., Robert, J. M., and Voigt, H. F. 1988b. Response properties of cochlear nucleus neurons in relationship to physiological mechanisms. In Edelman, G. M., Gall, W. E., and Cowan, W. M., editors, Auditory Function, pages 277–312, New York. Wiley.